buildings

MDPI

Article

Experimental Study on Seismic Repair of Prefabricated Single-Beam Column Joints in Modern Chinese Traditional-Style Buildings

Zhanjing Wu [1,2], Xinwu Wang [1,2], Fengxia Li [1,2,*], Jinshuang Dong [3], Xicheng Zhang [4] and Haisu Sun [1,2]

[1] School of Intelligent Construction and Civil Engineering, Luoyang Institute of Science and Technology, Luoyang 471023, China; zhanjing_wu@lit.edu.cn (Z.W.); 200900600357@lit.edu.cn (X.W.); 200900600405@lit.edu.cn (H.S.)
[2] International Union Laboratory of New Civil Engineering Structure of Henan Province, Luoyang 471023, China
[3] College of Civil Engineering and Architecture, Hainan University, Haikou 570228, China; 993629@hainanu.edu.cn
[4] School of Civil Engineering, Xi'an University of Architecture & Technology, Xi'an 710055, China; zhangxicheng@xauat.edu.cn
* Correspondence: 200900600371@lit.edu.cn

Abstract

To investigate the feasibility and effectiveness of seismic repair for prefabricated single-beam column joints in modern Chinese traditional-style buildings (MCTBs), low-cycle reversed loading tests were conducted on two original joints with different T-stub web thicknesses and one repaired joint. A repair strategy was proposed in which damaged T-stub connectors were removed and replaced with welded end-plate connections. The seismic behavior of the joints, including failure mode, hysteretic response, skeleton curve, stiffness degradation, ductility, energy dissipation capacity, and seismic performance comparison between the original and repaired joints, was systematically evaluated. In addition, a refined finite element model was established using ABAQUS and validated against the experimental results to investigate the stress distribution, deformation characteristics, and load-transfer mechanism of the joints. The results indicate that damage in the original joints was mainly concentrated in the T-stub connection region, while the beam and column members remained essentially intact, demonstrating an effective damage-control mechanism. Increasing the T-stub web thickness improved the load-carrying capacity, stiffness, and ductility of the joints. After repair, the load-transfer mechanism changed from a blind-bolted T-stub connection to a welded end-plate connection, resulting in a different damage evolution pattern and failure mode. Nevertheless, the repaired joint exhibited stable hysteretic behavior, satisfactory deformation capacity, and favorable energy dissipation performance. Compared with the original joint, the repaired specimen achieved a moment capacity comparison ratio of approximately 116%, stiffness comparison ratios exceeding 120%, and an energy dissipation comparison ratio of approximately 148%. The finite element results agreed well with the experimental observations and further revealed the evolution of stress concentration regions and load-transfer paths before and after repair. The present experimental results demonstrate the feasibility of the proposed repair method for rehabilitating damaged joints while maintaining satisfactory seismic performance without replacing the primary beam and column members. The proposed repair strategy therefore provides a practical and efficient solution for the post-earthquake rehabilitation of prefabricated joints in MCTBs.

Check for updates

Academic Editor: Gabriele Milani

Received: 19 June 2026
Revised: 17 July 2026
Accepted: 20 July 2026
Published: 21 July 2026

Copyright: © 2026 by the authors. Licensee MDPI, Basel, Switzerland. This article is an open access article distributed under the terms and conditions of the Creative Commons Attribution (CC BY) license.

Keywords: modern Chinese traditional-style buildings; prefabricated single-beam column joints; seismic performance; seismic repair; low-cycle reversed loading; finite element analysis

1. Introduction

With the increasing demand for the preservation of traditional architectural culture and the advancement of modern construction technologies, steel Modern Chinese traditional-style buildings (MCTBs) have been widely adopted due to their combined advantages of architectural authenticity and structural efficiency. Compared with conventional timber structures, steel structures exhibit superior load-carrying capacity, enhanced seismic performance, shorter construction periods, and improved durability, making them suitable for large-span, large-space, and complex roofing systems. In MCTBs, circular hollow section (CHS) columns are commonly employed to satisfy the geometric and aesthetic requirements of traditional architectural forms in beam–column systems [1]. A schematic of a modern Chinese traditional-style building is presented in Figure 1.



(**a**) (**b**)

Figure 1. Traditional Chinese-style building. (**a**) pavilion-style building; (**b**) hall-style building.

Existing studies have primarily focused on fully welded beam–column joints, in which stiffening ribs and diaphragm plates are introduced to ensure reliable load transfer between steel beams and CHS columns [2–4]. To further enhance seismic resistance and energy dissipation capacity, supplemental damping devices such as viscous dampers have also been integrated into joint regions to control seismic responses [5–8]. These studies demonstrate that both welded connections and damper-assisted systems can achieve satisfactory seismic performance for MCTBs. However, welded connections still present several limitations in practical applications. The complex joint detailing requires extensive on-site welding, which imposes strict demands on construction conditions and welding quality control. Moreover, many MCTBs are located in historical districts, scenic areas, or heritage conservation zones, where construction space is restricted and welding operations are difficult to implement. More critically, welded joints are prone to brittle fracture and local damage under severe earthquakes, and post-earthquake repair is often time-consuming and costly, limiting rapid functional recovery.

With the development of prefabricated steel construction, bolted connections have become an attractive alternative due to their ease of installation, quality control, and post-earthquake reparability. However, for closed-section members such as CHS columns, conventional bolted connections are difficult to apply because internal bolt installation

is not feasible. To overcome this limitation, blind bolt technology has been introduced as an effective solution for connecting closed-section members [9–19]. Previous studies have demonstrated the favorable cyclic behavior and mechanical characteristics of blind-bolted end-plate connections to tubular members [20–22]. Based on this concept, blind bolts combined with T-stub components have been proposed to form prefabricated beam–column joints suitable for CHS columns, providing a promising alternative for modular construction of MCTBs.

Our previous studies investigated blind-bolted T-stub beam-column joints for steel MCTBs. Prior studies examined blind-bolted T-stub beam-column joints in steel MCTBs. The results indicated that plastic deformation of the T-stub components can effectively dissipate seismic energy, while damage is concentrated in replaceable connection elements, thereby protecting the main beam and column members [23]. However, further experimental observations revealed that under large cyclic deformations, local bearing deformation occurs around the blind bolt holes in CHS columns. Direct replacement of damaged T-stub components may therefore affect connection accuracy and subsequent mechanical performance, which poses challenges for post-earthquake recovery [24].

In recent years, seismic design philosophy has shifted from conventional performance objectives toward functional recovery-based design. For critical infrastructure, public buildings, and heritage-related structures, rapid restoration of functionality after earthquakes is essential. Consequently, improving structural resilience through damage control, reduced repair cost, and shortened downtime has become a key research direction in earthquake engineering. The design concept of replaceable energy-dissipating components is to concentrate inelastic deformation in sacrificial elements, while limiting damage accumulation in primary structural members. Post-earthquake repair through component replacement is an effective strategy for restoring the functionality of damaged structures. In this context, replaceable energy-dissipating systems, such as T-stub connections, buckling-restrained fuses, and repairable beam–column joints, have been developed to improve the seismic resilience of steel structures. Blind-bolted end-plate systems have also been investigated for their potential advantages in prefabrication and damage control under extreme loading conditions [25].

Various replaceable connection systems have been proposed for steel beam–column joints, including replaceable beam segments, angle connections, cover plate connections, and T-stub connections. Among them, T-stub connections are widely studied due to their simple configuration, clear load transfer mechanism, and ease of replacement. Men et al. [26] proposed steel beam–column joints with replaceable T-stub components, demonstrating that plastic damage was concentrated in the T-stub elements and seismic performance could be effectively restored by replacement. Li et al. [27] developed fragility and resilience evaluation models for steel frames with replaceable T-stub connections, showing significant improvements in post-earthquake repair efficiency and life-cycle performance. Chen et al. [28] proposed joints with buckling-restrained fuse components, which effectively enhanced energy dissipation capacity and post-earthquake reparability. However, most existing studies focus on conventional steel frame systems. Research on blind-bolted beam–column joints for steel MCTBs remains limited, particularly regarding their post-earthquake repair ability and functional recovery mechanisms [29–34].

To address the seismic damage and post-earthquake repair of prefabricated single-beam column joints in MCTBs, this study proposes a repair strategy for blind-bolted T-stub connections. After severe damage occurs in the T-stub components [35], the damaged T-stubs and blind bolts are removed and replaced by welded end-plate connections to restore the joint load-transfer mechanism and structural functionality. Low-cycle reversed loading tests were conducted on both original and repaired joints to investigate their

failure modes, hysteretic behavior, stiffness degradation, ductility, and energy dissipation capacity. In addition, a validated finite element model was developed to simulate the stress distribution and deformation characteristics of the joints under cyclic loading. Based on experimental and numerical results, the seismic performance of the original and repaired joints was evaluated in terms of strength, stiffness, and energy dissipation comparison ratios, providing a reference for the seismic design and repair of prefabricated single-beam column joints in MCTBs.

2. Experimental Program

2.1. Specimen Design

The prefabricated T-stub beam–column joint investigated in this study was developed based on previous studies of all-welded steel joints in MCTBs [3] and blind-bolted T-stub connections [23,24]. The design of the T-stub connector considered both the structural requirements of MCTBs and fabrication feasibility, including the connection geometry, blind-bolt arrangement, and sectional cutting process of steel members. The dimensions of the T-stub connector were determined considering both the structural requirements of modern Chinese traditional-style buildings and fabrication feasibility. To investigate the seismic performance and post-earthquake repair behavior of the proposed joint, two single-beam blind-bolted T-stub beam–column joint specimens, designated as T1 and T2, were designed and fabricated. Specimen T1 was used for comparative reference, while specimen T2 was selected for subsequent repair testing. After completing the low-cycle reversed loading test on T2, the damaged T-stub components and associated blind bolts were removed and replaced with a welded end-plate connection, forming the repaired specimen R1. The main geometric parameters of the specimens are summarized in Table 1 and Figure 2.

Table 1. Specimen details.

Specimen	Connector Type	Circular Pipe (mm)	Rectangular Tube (mm)	T-Stub (mm)	End Plate (mm)	Beam (mm)
T1	T-stub	273 × 12	150 × 10	T210 × 130 × 8 × 12	/	HN200 × 130 × 6 × 8
T2	T-stub	273 × 12	150 × 10	T210 × 130 × 9 × 14	/	HN200 × 130 × 6 × 8
R1	End plate	273 × 12	150 × 10	/	196 × 130 × 9	HN200 × 130 × 6 × 8

Note: T210 × 130 × 8 × 12 denotes T-stub with an overall height of 210 mm, flange width of 130 mm, web thickness of 8 mm, and flange thickness of 12 mm.

2.1.1. Design of T-Stub Joints

The prototype of the test specimen was derived from a beam–column joint in a second-class hall-type steel modern Chinese traditional-style building, and the geometric scale was determined based on the traditional ts'ai-fen modular system described in Yingzao Fashi [36]. A geometric scaling ratio of 1:2.6 was adopted in combination with available steel section specifications.

The proposed joint consists of CHS columns, H-shaped steel beams, T-stub connectors, blind bolts, and leveling plates, as illustrated in Figure 3. A box-shaped transition component is installed inside the CHS column to connect the upper traditional architectural bracket system and transfer vertical roof loads, thereby forming a variable cross-section composite load-bearing system characteristic of MCTBs. The RHS column is connected to the CHS column through horizontal and vertical stiffeners. During fabrication, the RHS column and the horizontal and vertical stiffeners were first assembled and welded as an integrated transition component, which was subsequently connected with the CHS

column. The stiffeners were welded to both the RHS column and the inner surface of the CHS column, providing a reliable load-transfer path between the internal box section and the external circular tube. The sectional configuration, welding details, and assembly relationship of the transition column are illustrated in Figure 2c, Figure 3c, and Figure 3d, respectively. The corresponding fabrication process of the transition column is shown in Figure 4b. This type of transition column configuration has also been experimentally investigated and validated in previous research [2].

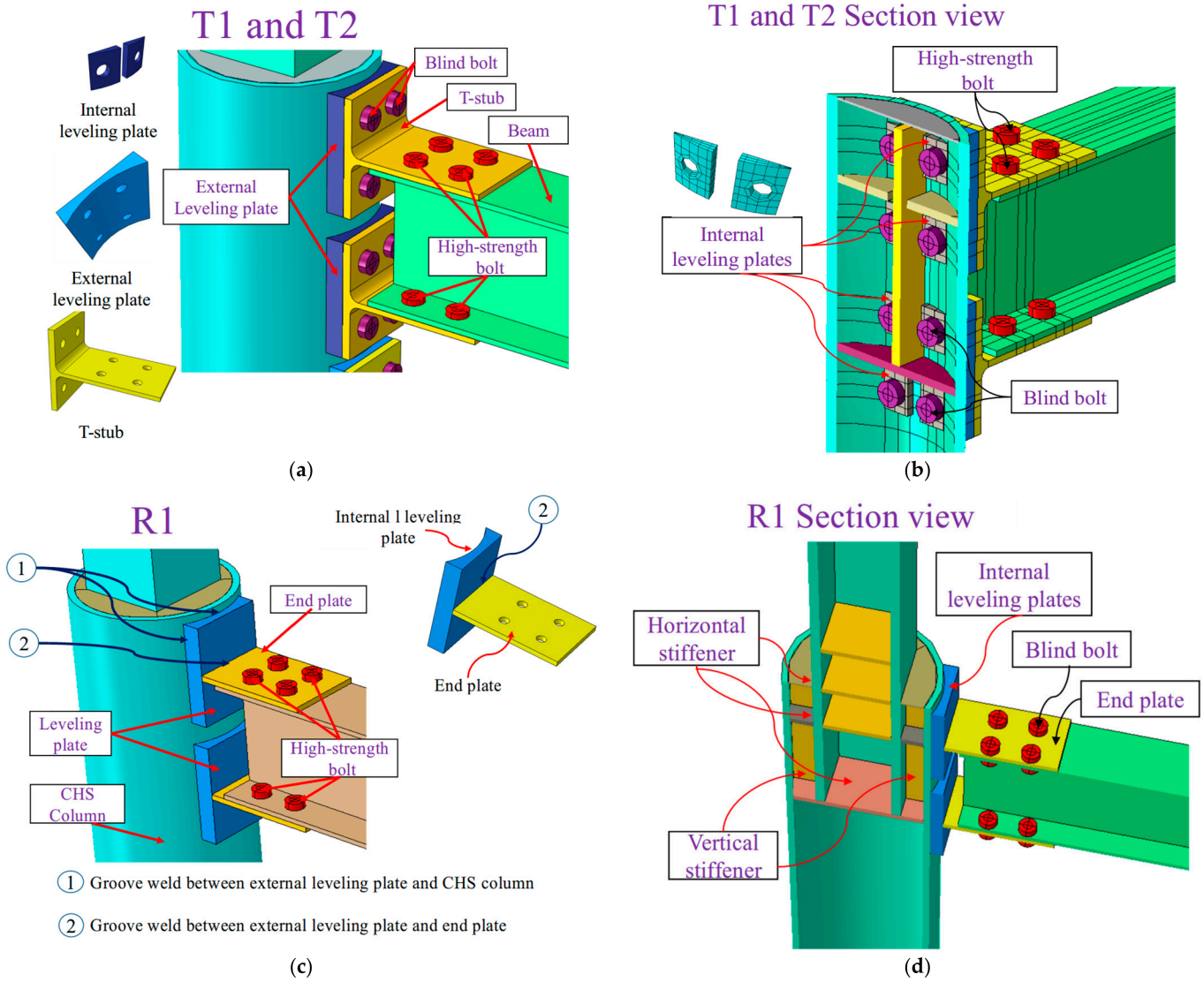
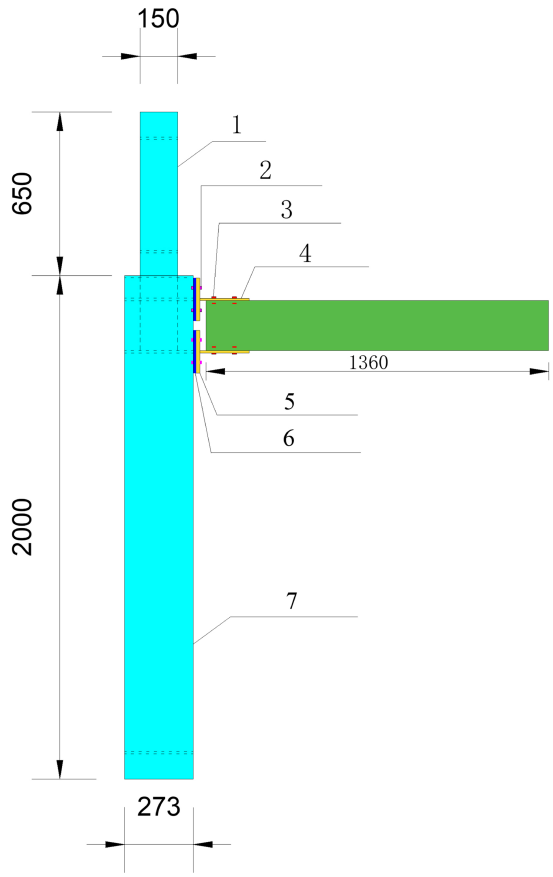


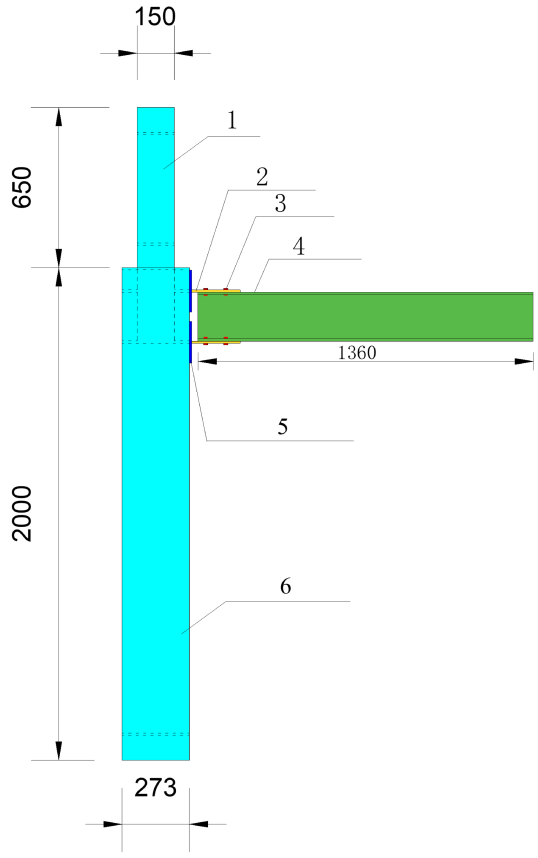
Figure 2. Prefabricated beam–column joint for steel MCTBs. (**a**) Schematic diagram of T1 and T2; (**b**) Section view of T1 and T2; (**c**) Schematic diagram of R1; (**d**) Section view of R1.

The design of the specimens follows the Steel Structure Design Standard (GB 50017–2017) [37] and the Code for Seismic Design of Buildings (GB 50011–2010) [38]. The CHS column is Φ273 × 12 mm seamless steel tube with a height of 2000 mm, while the H-section beam is H200 × 130 × 6 × 8 with a length of 1360 mm. The axial load ratio is set to 0.20, corresponding to an applied axial force of 275 kN.



1— Rectangular tube 150×150×10
2— M16 Blind bolt
3— M16 High-strength bolt
4— *Lan-e* (Beam) H200×130×9×14
5— T-stub 210×130×9×14
6— Leveling plate
7— Circular pipe Φ273×12

(**a**)



1— Rectangular tube 150×150×10
2— End plate196×130×9
3— M16 High-strength bolt
4— *Lan-e* (Beam) H200×130×9×14
5— Leveling plate
6— Circular pipe Φ273×12

(**b**)

Figure 3. *Cont.*

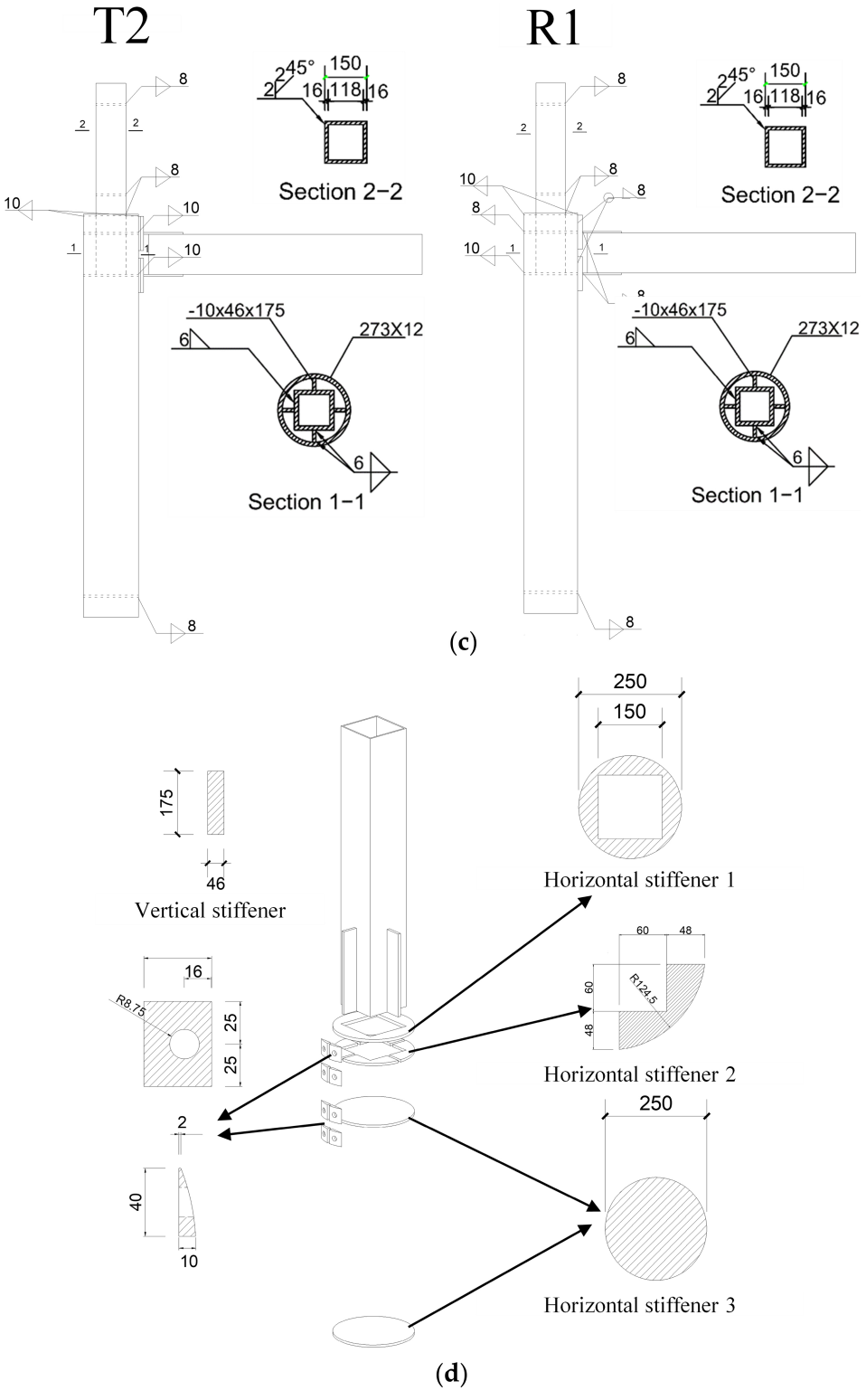


Figure 3. Dimensions and welding details of the specimens. (**a**) Dimensions of specimen T2; (**b**) Dimensions of specimen R1; (**c**) Welding details of specimens; (**d**) Exploded views of column.

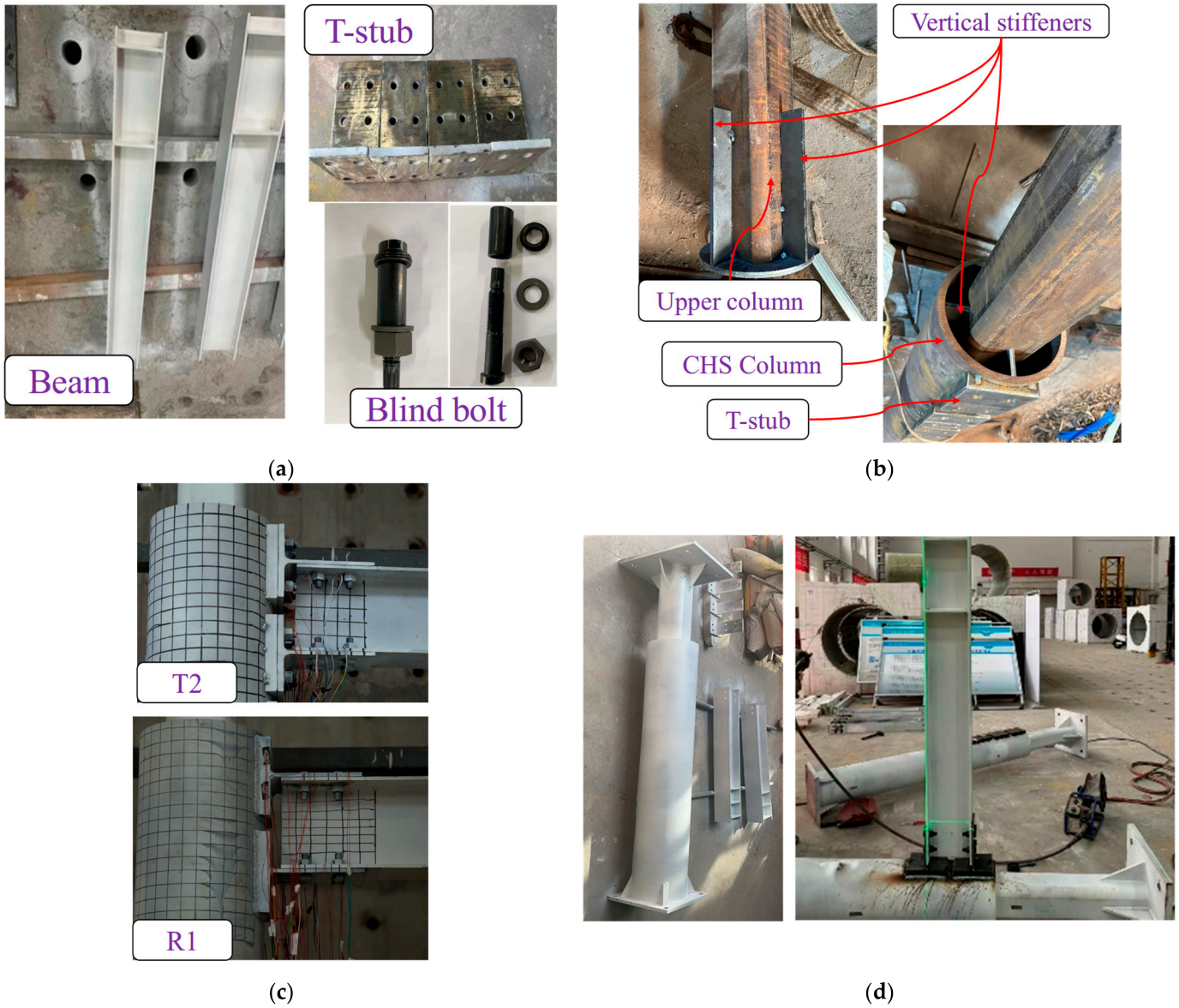


Figure 4. Fabrication and assembly of the specimens. (**a**) Prefabricated components; (**b**) Column; (**c**) Comparison of connection; (**d**) Assembly of the specimen.

To ensure effective load transfer and local stability in the joint region, vertical stiffeners are installed at the beam loading zone, and both horizontal and vertical stiffeners are arranged inside the CHS column. The key connection components include the T-stub connector, blind bolts, and beam-end high-strength bolts, designed in accordance with relevant design specifications for bolted connections. For architectural compatibility, the width of the T-stub is taken equal to the beam flange width (130 mm), and Q235B steel is used. Based on bending in the flange, shear in the web, and bolt connection demands, the load-bearing capacity of the T-stub and high-strength bolts was verified. The results indicate that both the 9 mm thick T-stub and M16 grade 10.9 bolts satisfy the strength requirements with sufficient safety margins. To investigate the influence of T-stub web thickness on seismic performance, two blind-bolted T-stub beam–column joint specimens were designed. Specimen T1 adopted an 8 mm thick T-stub web, while T2 adopts a 9 mm thickness, with all other parameters kept identical. The detailed dimensions of the specimens are shown in Figures 3a and 3b, while the welding details and transition column configuration are provided in Figures 3c and 3d, respectively.

The thickness of the T-stub connector was determined considering both fabrication feasibility and the intended damage-control mechanism. In this study, the T-stub connector was fabricated by cutting commercially available H-section steel rather than being independently manufactured. According to the joint configuration requirements and the arrangement of blind bolts, the flange height of the T-stub was determined as 170 mm, resulting in a total height of approximately 210 mm for the T-stub section. Therefore, an H-section steel with a height of no less than 420 mm was required to obtain a symmetric T-stub through cutting along the neutral axis. Among the available steel sections, HN450 × 200 was selected, and the resulting T-stub web thicknesses were 8 mm and 9 mm, which satisfied both geometric and strength requirements. In addition, the selection of the T-stub thickness was also related to the desired damage-control mechanism. Previous experimental investigations on blind-bolted T-stub beam–column joints demonstrated that excessively thick T-stub connectors may change the governing failure mode from T-stub yielding to bolt pull-out or local damage of the column wall [23,24]. Such failure modes are unfavorable for achieving a replaceable energy-dissipating mechanism. Therefore, the T-stub thickness should not be increased excessively, and the connector should be designed to yield before the primary beam and column members are significantly damaged.

It should be noted that the present study adopted a geometric scaling ratio of 1:2.6. Although the scaled specimens are appropriate for investigating the overall seismic behavior and repair feasibility of the proposed joints, local behaviors involving weld fracture, blind-bolt bearing, and CHS column wall deformation may exhibit scale effects. Therefore, further full-scale validation is required before extending the present findings to engineering practice.

2.1.2. Design of the Repaired Joint

To verify the feasibility of the proposed post-earthquake repair strategy, the damaged T-stub and blind bolts of specimen T2 were removed after the low-cycle reversed loading test. However, direct reconstruction of the original T-stub joint was not feasible because the internal leveling plates inside the closed-section CHS column could not be accurately repositioned after cyclic loading. Therefore, the damaged connection region was replaced by a welded end-plate connection, forming the repaired specimen R1. Specimen R1 was reconstructed from the previously tested specimen T2 rather than fabricated using new components. This approach was adopted to reproduce an actual post-earthquake repair scenario. In this case, the repaired joint inherently considers the possible effects of previous damage, residual deformation, and construction limitations during repair. Conversely, if a new specimen were fabricated, the influence of the previous damage state would be eliminated, and the obtained response would represent the performance of a newly constructed joint rather than a repaired connection. Therefore, using the damaged T2 specimen as the basis for R1 provides a more realistic evaluation of the post-earthquake seismic performance.

Considering that specimen T2 adopted a 9 mm thick Q235B T-stub connector, a 9 mm thick Q235B end plate was adopted for the repaired specimen R1. During the repair process, the damaged T-stub and the original blind-bolted connection components were removed. It should be noted that the external leveling plate of specimen T2 was not damaged during the cyclic loading test because the joint design ensured that seismic damage was concentrated in the replaceable T-stub component. However, the original external leveling plate was not reused in specimen R1 because it was specifically designed for the blind-bolted T-stub connection, with bolt holes provided for blind-bolt installation. In contrast, the repaired end-plate connection required a non-perforated external leveling plate to provide a suitable welding surface and ensure reliable force transfer, as shown in Figures 2 and 4. Therefore, the original perforated external leveling plate was replaced by a new non-perforated

external leveling plate. The curved surface of the new external leveling plate was connected to the CHS column using groove welding, while the flat surface was welded to the end plate. The end plate was then connected to the beam flange using high-strength bolts, forming a welded–bolted hybrid connection. The configuration of the repaired specimen R1 is illustrated in Figure 2c,d, while the detailed dimensions and welding details of R1 are provided in Figure 3.

2.2. Fabrication and Assembly of Specimens

To ensure fabrication quality, all components were manufactured and assembled in accordance with the Code for Acceptance of Construction Quality of Steel Structures (GB 50205–2020) [39]. A combination of factory prefabrication and on-site assembly was adopted, as illustrated in Figure 4. The joint consists of a CHS column with an embedded inner box column. The CHS column ($\Phi 273 \times 12$ mm) serves as the primary load-bearing member, while the upper box column ($150 \times 150 \times 10$ mm) is centrally arranged within the CHS column to connect the upper traditional-style bracket system and transfer vertical loads. Horizontal and vertical stiffeners were installed between the box column and CHS column to ensure effective force transfer. All primary components were prefabricated in the factory. The column base and internal horizontal stiffeners were welded into an integrated unit, while the box column and vertical stiffeners were prefabricated as a subassembly. Beam-end vertical stiffeners were welded to the H-shaped steel beam. Leveling plates and T-stub connectors were manufactured by laser cutting to ensure dimensional accuracy and surface contact quality. To monitor strain responses of the blind bolts, access holes were reserved on the CHS column at corresponding positions for wiring strain gauges. A 30 mm $\times$ 30 mm grid was marked on the joint surface to record deformation development during testing. During on-site assembly, the beam and column were first positioned, followed by installation of leveling plates, blind bolts, T-stub connectors, and high-strength bolts, which were then tightened to the specified pretension force.

For the repair study, specimen T2 was subsequently repaired to form specimen R1, as shown in Figure 4. The repair process retained the original CHS column, H-shaped beam, and beam-end high-strength bolt system. The original perforated external leveling plate was removed and replaced with a new non-perforated leveling plate. Only the damaged T-stub connector and corresponding blind bolts were removed before installing the welded end-plate connection. The remaining beam, column, and plate components were inspected to confirm the absence of significant plastic deformation. A new 9 mm thick Q235B steel end plate, designed with the same thickness as the web of the original T-stub, was then fabricated and used to replace the damaged connector. The end plate was welded to the CHS column-side component and connected to the H-shaped beam flange using the original high-strength bolts, forming a hybrid bolted–welded connection system.

2.3. Material Testing

To obtain the actual mechanical properties of the materials used in the specimens, tensile coupon tests were conducted prior to the structural tests. Specimens were extracted from the same batch of Q235B steel. The preparation of specimens and testing procedures were carried out in accordance with the Metallic materials-Tensile testing (GB/T 228.1–2010) [40]. Standard tensile coupons were prepared according to the actual plate thickness of each structural component, including the CHS column, H-shaped steel beam, end plates, T-stub connectors, and stiffeners. For each material type, at least three specimens were tested, and the average values were adopted as the representative material properties. The tensile tests provided key mechanical parameters, including yield strength, ultimate tensile strength, elastic modulus, and elongation after fracture. The measured

results are summarized in Table 2. These experimentally obtained material properties were directly used in subsequent experimental analysis and finite element modelling to ensure consistency between numerical simulation and physical tests.

Table 2. Mechanic performance indexes.

Type	Thickness (mm)	f_y (MPa)	f_u (MPa)	E_s ($\times 10^5$ MPa)	Δ (%)
Tube	12	288	388	1.92	/
Beam flange	8	252	440	1.99	32.2
Beam web	6	280	442	1.96	35.1
T-stub flange (T2)	14	268	447	1.96	34.5
T-stub web (T2)	9	271	445	2.16	37.5
T-stub flange (T1)	12	283	483	2.21	39.5
T-stub web (T1)	8	330	450	2.15	36.3
End plate (R1)	9	270	440	2.19	34.3

2.4. Experimental Setup

The experimental setup is shown in Figure 5. The column base was modeled as a pinned boundary condition and connected to the laboratory reaction floor through anchor bolts. A 200-ton electro-hydraulic servo actuator (Beijing Fluid Control System (FCS) Corp., Beijing, China) was attached to the column top via a loading fixture to apply a constant axial load. A 50-ton electro-hydraulic servo actuator (Beijing Fluid Control System (FCS) Corp., Beijing, China) was connected to the free end of the H-shaped steel beam to impose cyclic lateral displacement. During testing, the axial load at the column top was kept constant to simulate the gravity effect from the upper structure, while cyclic lateral displacement was applied at the beam end to simulate seismic actions. The adopted boundary conditions and loading configuration are consistent with the mechanical behavior of actual beam-column joints. The loading protocol is illustrated in Figure 6. Before yielding, load-controlled cycles were applied with one cycle per loading step. During the loading process, the strain responses of the measuring points installed in the critical regions of the T-stub connector were continuously monitored. Once the measured strain reached the yield strain of the steel material, the corresponding beam-end displacement was recorded and defined as the yield displacement Δ_y. The loading scheme was then switched to displacement control. In the displacement-controlled stage, incremental displacement amplitudes of 1 Δ_y, 2 Δ_y, 3 Δ_y, 4 Δ_y, and 5 Δ_y were applied sequentially, with three cycles at each amplitude. Positive loading corresponds to actuator pushing, while negative loading corresponds to pulling; one full positive–negative cycle is defined as one loading cycle. The test was terminated when the load capacity degraded to 85% of the peak strength or when severe damage occurred such that further loading could not be sustained.

2.5. Measurement Scheme

To capture the mechanical response of the joints under low-cycle reversed loading, a comprehensive measurement system consisting of load, displacement, and strain measurements was established, as shown in Figures 6 and 7. The load was recorded in real time using the built-in sensors of the electro-hydraulic servo actuators. Displacement measurements were used to obtain the global deformation of the specimens and the rotational behavior of the joints. Displacement transducers were installed at the column top, column base, and beam end to measure lateral column displacement, beam-end displacement, and joint rotation, respectively. In addition, wire-type displacement transducers were arranged in the joint region to measure the relative deformation between the beam and column. Strain measurements were mainly arranged at key locations, including the T-stub connectors,

blind bolts, beam flanges, beam webs, and the column top and base. A denser arrangement was adopted in the joint core region to capture strain evolution and the development of plastic zones. All load, displacement, and strain signals were synchronously recorded using a DH3816N static strain acquisition system (Jiangsu Donghua Testing Technology Co., Ltd., Jingjiang, China). To facilitate the observation of deformation patterns and crack propagation, the specimen surfaces were painted prior to testing, and a 30 mm × 30 mm grid was marked in the joint region.

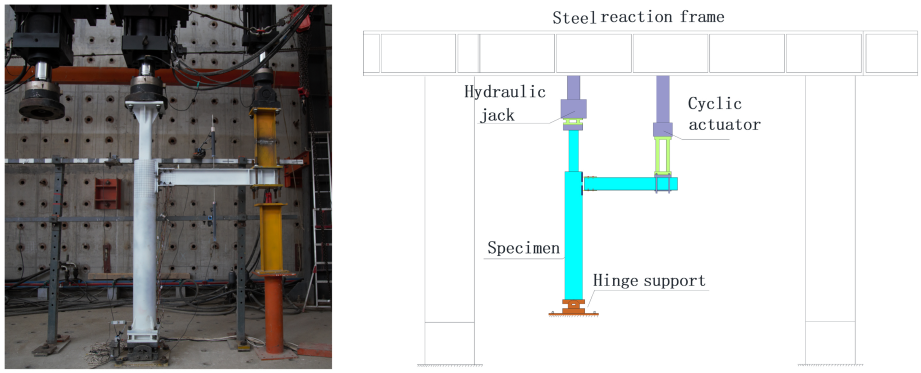


Figure 5. Test setup. (**a**) On-site photograph; (**b**) Schematic diagram.

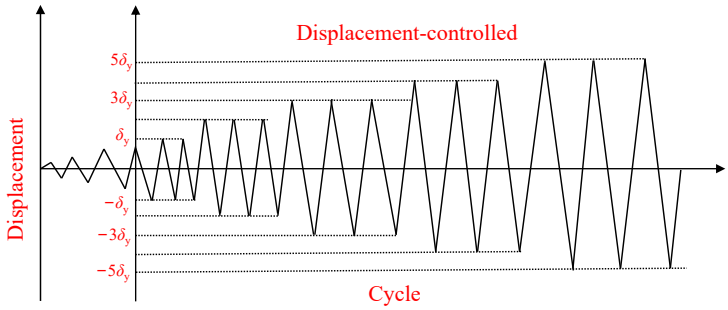


Figure 6. Loading protocol.

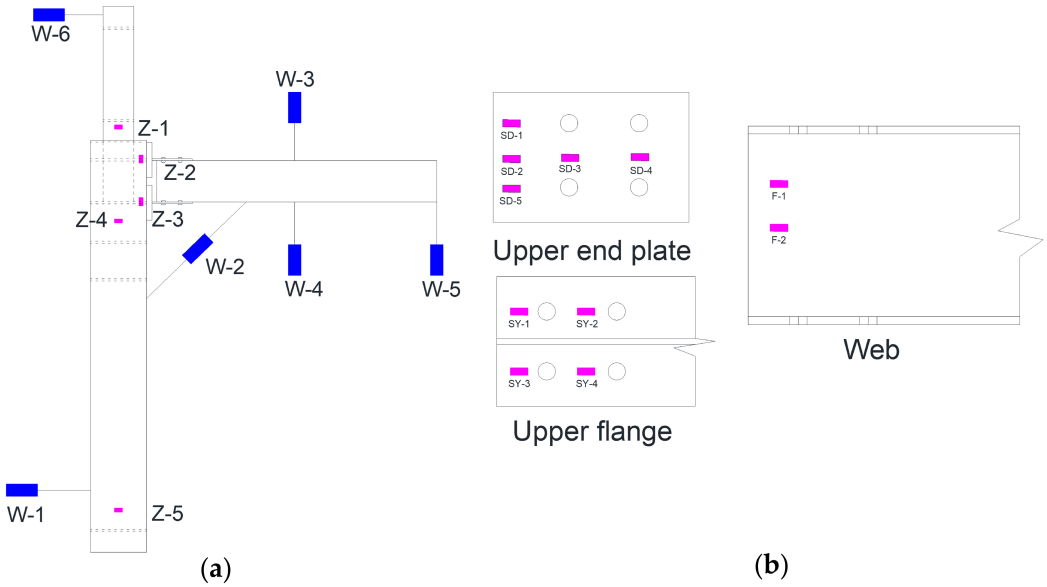


Figure 7. Layout map of measurement points. (**a**) Displacement gauge layout; (**b**) Strain gauge arrangement.

3. Test Results

3.1. Failure Modes

Specimens T1 and T2 exhibited consistent damage evolution under low-cycle reversed loading, with failure governed by fracture of the T-stub connectors after yielding. Since T2 served as the reference specimen for the subsequent repair study, the following analysis focuses on T2. At the initial loading stage, all components remained in the elastic range, and no visible damage was observed in the joint region. When the displacement reached $\pm$48 mm (2 Δ_y), yielding first occurred in the T-stub web and beam flange, accompanied by slight opening between the T-stub and the leveling plate. As the displacement increased to $\pm$72 mm (3 Δ_y), interface slip progressively developed, initial slip of the high-strength bolts was observed, and local out-of-plane deformation occurred at the edge of the T-stub flange, indicating stable plastic development of the joint. At $\pm$96 mm (4 Δ_y), cracking initiated at the lower T-stub flange-web transition zone and propagated under cyclic loading. When the displacement reached $\pm$120 mm (5 Δ_y), a pronounced crack developed at the upper flange–web junction of the T-stub, leading to final fracture and significant strength degradation of the joint.

The final failure of T2 was characterized by fracture at the flange-web connection of the T-stub, tensile deformation of blind bolts, and progressive interface slip. In contrast, the beam, column, and leveling plates remained essentially elastic without noticeable plastic deformation or local instability. These results indicate that plastic deformation was effectively concentrated in the T-stub connectors, achieving the intended damage-control mechanism. The repaired specimen R1, formed by replacing the damaged T-stub with a welded end-plate connection, exhibited a different damage evolution pattern. In the load-controlled stage, slight slip was observed at the beam–end-plate interface at approximately 15 mm displacement. At 18 mm, initial local deformation occurred in the beam web. When the displacement reached 24 mm, yielding was first detected at the end-plate–welded connection region, which was defined as the yield displacement, after which the loading mode was switched to displacement control. At 2 Δ_y (48 mm), yielding developed in the beam upper flange, and interface slip between the beam and end-plate further increased. In the 3 Δ_y–4 Δ_y range (72–96 mm), plastic deformation accumulated in the end-plate region, accompanied by intensified interface slip, indicating stable energy dissipation behavior. During the later cycles at 4Δ_y, pronounced frictional behavior was observed, suggesting progressive damage accumulation. At 5 Δ_y (120 mm), a sudden strength degradation occurred during the second loading cycle, and fracture of the weld between the upper end-plate and leveling plate was observed, leading to termination of the test.

Compared with specimen T2, plastic deformation in R1 shifted from the T-stub connector to the end-plate and weld regions. The failure mode transformed from T-stub fracture to weld failure, indicating a redistribution of the load transfer path after repair. Nevertheless, the joint maintained a stable energy dissipation mechanism, while the beam and column members remained essentially elastic, providing a structural basis for post-earthquake functionality recovery. The failure processes of specimens T2 and R1 are shown in Figures 8 and 9, respectively.

To further verify the rationality of the T-stub design, the tensile resistance of the equivalent T-stub flange was estimated according to the equivalent T-stub model recommended in EN 1993-1-8 [41]. By substituting the geometric parameters of specimen T2 into the corresponding equations, the tensile resistance of the equivalent T-stub flange was calculated as 234 kN. During the experiment, the actuator load corresponding to the first yielding of the T-stub strain gauges was approximately 32 kN, which corresponds to an equivalent tensile force of approximately 227 kN in the T-stub flange. The close agreement between the analytical prediction and the experimental demand indicates that the adopted T-stub

dimensions were appropriately designed and that yielding initiated as intended in the T-stub connection region.

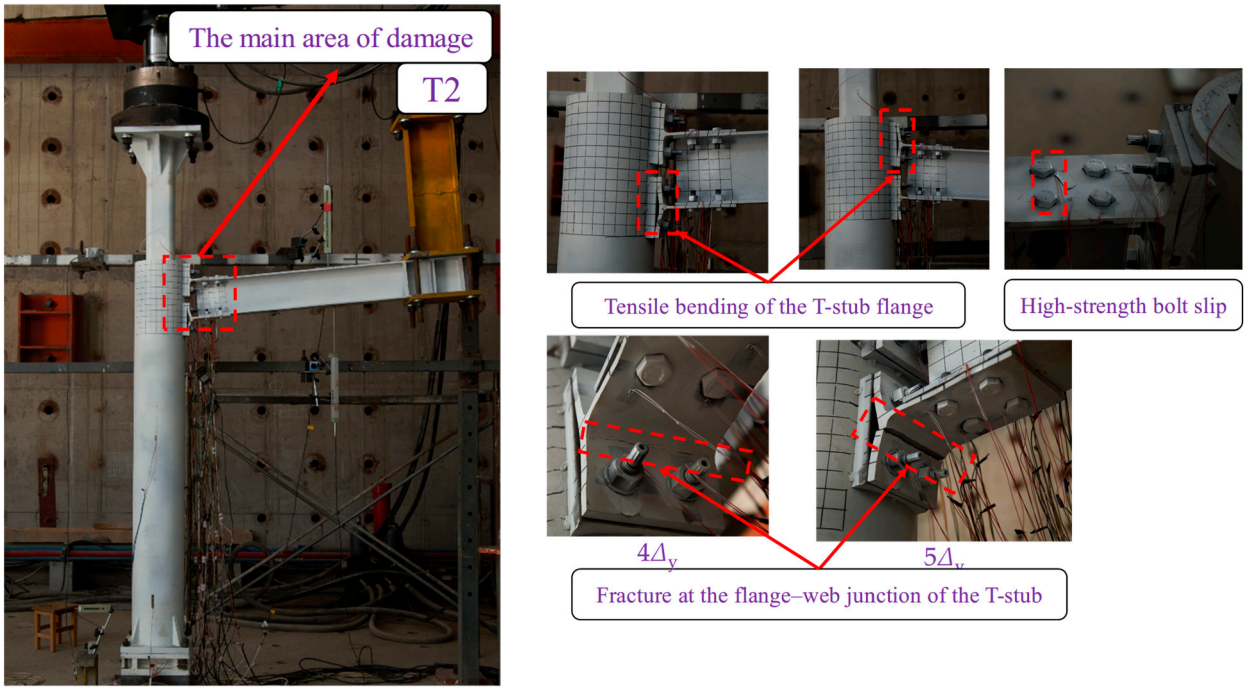


Figure 8. Failure modes of specimen T2. (**a**) Overall failure pattern; (**b**) Local failure details.

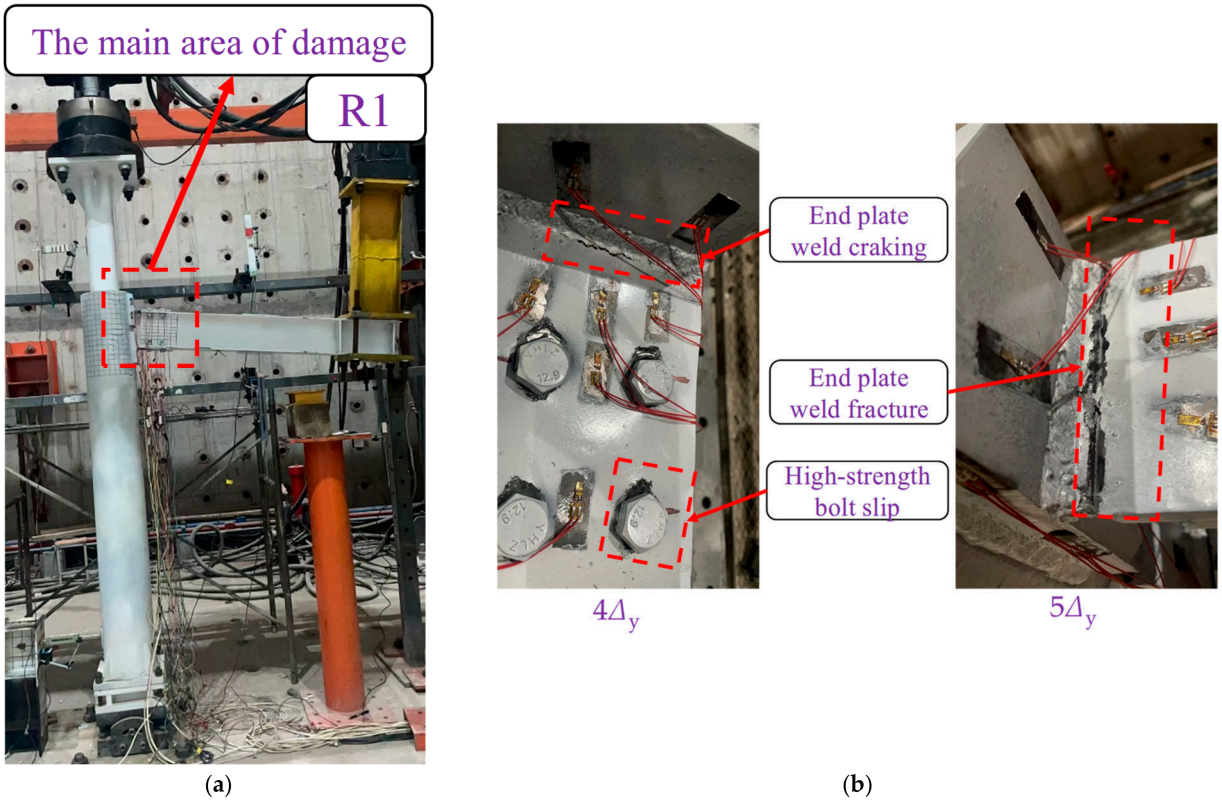


Figure 9. Failure modes of specimen R1. (**a**) Overall failure pattern; (**b**) Local failure details.

3.2. Hysteretic Behavior

The moment-rotation hysteretic responses of specimens are shown in Figure 10. All specimens exhibit stable hysteretic responses without obvious instability prior to reaching peak strength, indicating satisfactory deformation capacity and energy dissipation capacity of the joints. For specimens T1 and T2, the hysteretic loop area increases with increasing rotation amplitude, indicating progressive enhancement of energy dissipation capacity. Meanwhile, the T-stub connectors gradually enter the plastic stage, leading to cumulative plastic deformation and continuous stiffness degradation, as reflected by the reduction in loop slope. Near ultimate conditions, cracks initiate and propagate at the flange-web transition zone of the T-stub, resulting in strength degradation and a slight deterioration of the hysteretic response. Both T1 and T2 exhibit typical "bow-shaped" hysteretic loops with noticeable pinching effects. This behavior is primarily attributed to residual deformation of the yielded T-stub, gap opening induced by blind bolt deformation, and slip of high-strength bolts at the interfaces.

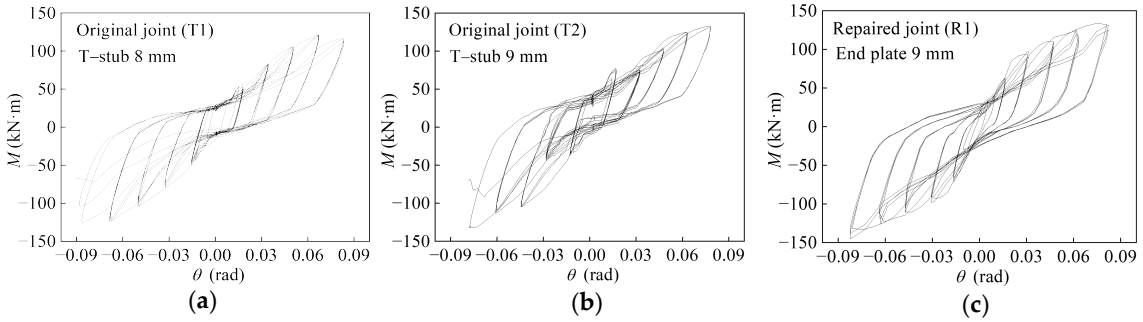


Figure 10. Hysteretic curves of specimens. (**a**) T1; (**b**) T2; (**c**) R1.

Compared with the T-stub specimens T2, the repaired specimen R1 exhibits similar overall hysteretic characteristics but more pronounced pinching behavior. This is due to slip of high-strength bolts at the beam-end-plate interface, progressive degradation of interfacial friction, and plastic deformation in the end-plate and weld regions, which collectively reduce both unloading and reloading stiffness. At large displacement amplitudes, stress concentration in the weld region intensifies, eventually leading to fracture at the weld between the upper end plate and leveling plate. This causes a sudden reduction in load-carrying capacity and an obvious descending branch in the hysteretic curves. From the overall response, plastic deformation in T1 and T2 is concentrated in the T-stub connectors, whereas in R1 it shifts to the end-plate and weld regions. Although the load transfer mechanism changes after repair, R1 still maintains stable hysteretic behavior and adequate energy dissipation capacity, demonstrating satisfactory seismic performance after replacement of the damaged T-stub.

In addition, comparison between T1 and T2 indicates that increasing the T-stub web thickness from 8 mm to 9 mm slightly enhances peak moment capacity and energy dissipation performance, suggesting that increasing connector stiffness improves the seismic behavior of the joint.

3.3. Skeleton Curve

The skeleton curves of specimens are shown in Figure 11. All specimens exhibit three typical stages, including an initial elastic stage, a nonlinear elasto-plastic stage, and a post-peak degradation stage. In the elastic stage, the moment increases linearly with rotation. With increasing deformation, stiffness decreases due to yielding of the connection region. After reaching the peak strength, all specimens enter the degradation stage. For specimens T1 and T2, plastic deformation is concentrated in the T-stub joints. Cracks

initiate at the flange-web junction and propagate with increasing rotation, leading to strength degradation. Compared with T1, specimen T2 shows higher peak moment and slightly larger rotation capacity, indicating that increased T-stub web thickness improves strength and deformation capacity.

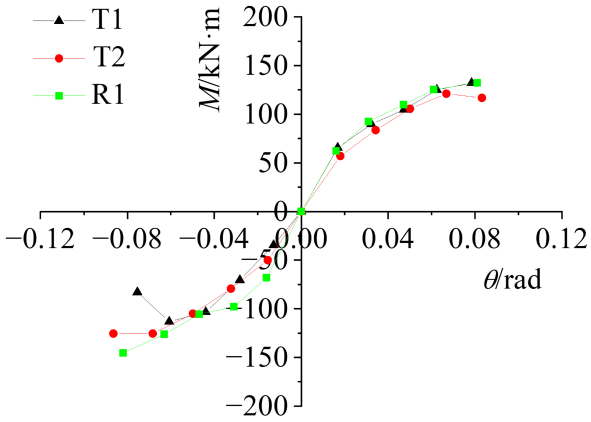


Figure 11. Skeleton curves.

For specimen R1, the skeleton curve shows a similar trend to that of T2, indicating that the basic load-transfer mechanism is maintained after repair. However, the initial stiffness differs slightly due to the change in connection type from blind-bolted T-stub to welded end-plate connection. Plastic deformation in R1 is concentrated in the end-plate and weld regions, and failure occurs due to weld fracture.

3.4. Ductility Analysis

The ductility coefficients of specimens are listed in Table 3. The ductility coefficient of the repaired specimen R1 is 2.61, which is only 5% lower than that of T2, indicating that the welded end-plate repair strategy can effectively maintain the plastic deformation capacity of the joint. Although the load transfer mechanism changes after repair, the ultimate deformation capacity of R1 remains comparable to that of the original specimen. Overall, all specimens exhibited stable deformation capacity after reaching the peak strength. For specimen R1, although weld fracture occurred during the final loading stage, the joint had already achieved an ultimate rotation of 0.081 rad and a ductility coefficient of 2.61 before the final failure. This indicates that the repaired joint achieved a comparable rotation capacity to the original specimen T2 before weld fracture.

Table 3. Ductility coefficient.

Specimens	Yield Rotation θ_y (Rad)	Ultimate Rotation θ_u (Rad)	μ
T1	0.032	0.084	2.62
T2	0.028	0.077	2.75
R1	0.031	0.081	2.61

Although specimen R1 exhibited slightly lower ductility than specimen T2, with the ductility coefficient decreasing from 2.75 to 2.61, the repaired joint still satisfied the deformation demand of the connection. The reduction in ductility was mainly associated with the change in failure mechanism. Compared with the progressive yielding and fracture of the T-stub connector in specimen T2, specimen R1 eventually failed by fracture of the weld connecting the end plate to the external leveling plate, resulting in a more abrupt strength degradation. Therefore, the proposed repair strategy represents a trade-off

between enhanced strength and stiffness and a less ductile failure mode. Nevertheless, the primary beam and column members remained essentially undamaged, indicating that the capacity-design objective of protecting the main structural members was still achieved, although the designated energy-dissipating component shifted from the replaceable T-stub connector to the welded end-plate connection.

The stiffness degradation curves of specimens are shown in Figure 12. The rotational stiffness of all specimens shows a continuous decreasing trend, indicating significant stiffness degradation. In the initial loading stage, the stiffness decreases rapidly, followed by a gradually reduced degradation rate. After entering the plastic stage, the stiffness further decreases due to the progressive accumulation of damage in the connection region. For the original specimens T1 and T2, stiffness degradation is primarily attributed to the development of plastic deformation in the T-stub connectors, slip at the blind-bolted interfaces, and the accumulation of residual deformation. Compared with T1, specimen T2 with a thicker T-stub web exhibits higher initial and overall stiffness, indicating that increasing the thickness of the T-stub web can effectively enhance the deformation resistance and delay stiffness degradation. In addition, specimens T2 and R1 exhibit relatively symmetric stiffness degradation characteristics in the two loading directions, indicating stable and predictable behavior of both the original and repaired joints under cyclic loading.

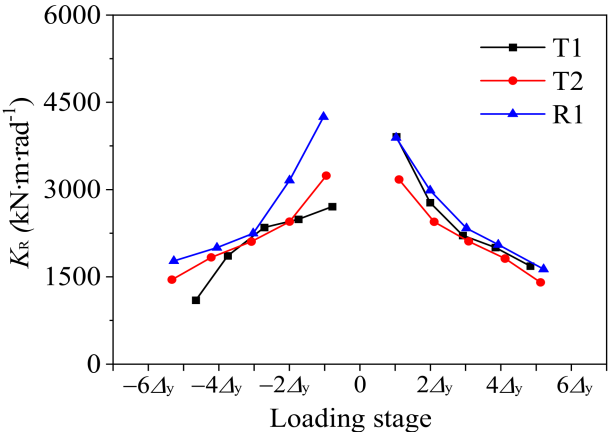


Figure 12. Stiffness degradation.

The stiffness degradation behavior of the repaired specimen R1 is generally similar to that of the original specimens. However, due to the change in connection configuration from a blind-bolted T-stub system to a welded end-plate bolted hybrid connection, the load transfer mechanism is modified. Under cyclic loading, plastic deformation develops in the end-plate region, slip occurs at the bolted interfaces, and damage gradually accumulates in the weld zone, leading to continuous stiffness degradation. Overall, all specimens exhibit a stable stiffness degradation process. Damage is mainly concentrated in the connection regions, while the beam and column members remain essentially elastic without significant damage.

3.5. Energy Dissipation Capacity

The cumulative energy dissipation of all specimens is summarized in Figure 13. With the increase in displacement amplitude, the cumulative energy dissipation of specimens continuously increases, indicating that the joints can effectively dissipate input energy through plastic deformation of the connection region and slip at the interfaces. For the original T-stub specimens, both T1 and T2 show a gradual increase in cumulative energy dissipation with loading progression. At a rotation level of 5 Δ_y, the cumulative energy dissipation reaches 8.68 kJ and 8.69 kJ for T1 and T2, respectively. The nearly identical final energy dissipation values indicate that, within the parameter range of this study,

the thickness of the T-stub web has a limited influence on the overall energy dissipation capacity of the joint. For the repaired specimen R1, the cumulative energy dissipation increases from 1.034 kJ at 1 Δ_y to 12.856 kJ at 5 Δ_y, which is higher than that of both T1 and T2. The higher cumulative energy dissipation of R1 should not be attributed directly to the more pronounced pinching or interface slip. Instead, specimen R1 maintained relatively high resisting forces at large deformation levels, while plastic deformation continued to develop in the end-plate and weld regions. Consequently, R1 accumulated more hysteretic energy over the complete loading history. Overall, all specimens exhibit satisfactory energy dissipation capacity. Among them, specimen R1 maintains a relatively higher energy dissipation level in the later loading stage. A more detailed comparison of energy dissipation will be further discussed in the subsequent section.

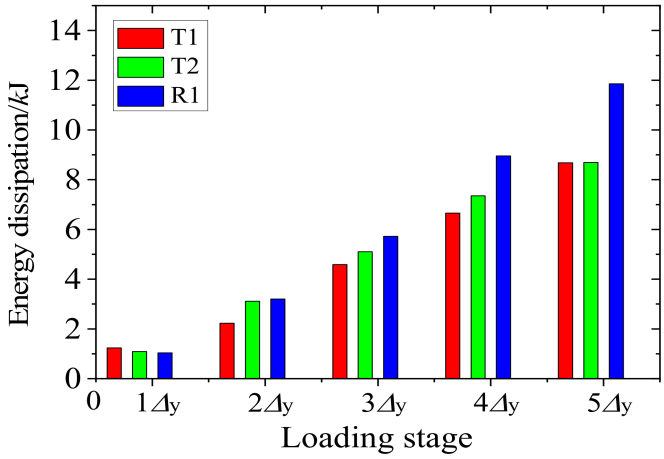


Figure 13. Cumulative energy dissipation of specimens.

The equivalent viscous damping ratios of specimens are summarized in Table 4. All specimens exhibit values greater than 0.13, indicating satisfactory energy dissipation capacity. Taking specimen T2 as an example, the damping ratio increases from 0.188 at 1 Δ_y to a peak value of 0.205 at 2 Δ_y, and then gradually decreases to 0.137 at 5 Δ_y. This indicates that in the early stage of plastic development, energy dissipation is dominated by yielding of the T-stub joint, interface slip, and local plastic deformation. However, with the propagation of cracks and accumulation of damage, the energy dissipation efficiency gradually decreases. In contrast, the repaired specimen R1 exhibits a relatively stable evolution trend. The equivalent viscous damping ratio increases gradually from 0.143 at 1 Δ_y to 0.165 at 5 Δ_y, without a noticeable degradation in the later loading stage. This behavior can be attributed to the fact that plastic deformation in R1 is mainly concentrated in the end-plate and weld regions, which continue to participate in energy dissipation even at large deformation levels, thereby maintaining a relatively stable damping capacity. Compared with T2, R1 shows slightly lower damping capacity in the early loading stage. However, as the displacement amplitude increases, the difference between the two specimens gradually reduces. At the 4 Δ_y and 5 Δ_y levels, the damping ratio of R1 even exceeds that of T2.

Table 4. Equivalent viscous damping coefficient of specimens.

Specimens	h_e				
	1 Δ_y	**2 Δ_y**	**3 Δ_y**	**4 Δ_y**	**5 Δ_y**
T1	0.199	0.241	0.162	0.150	0.136
T2	0.188	0.205	0.165	0.145	0.137
R1	0.143	0.161	0.158	0.169	0.165

3.6. Comparison of Seismic Performance Between the Original and Repaired Joints

Because specimens T2 and R1 adopt different connection configurations, the following indices are introduced to compare their seismic performance in terms of moment capacity, stiffness, and energy dissipation. These indices represent a performance comparison between the original blind-bolted T-stub joint and the repaired welded end-plate joint, rather than a measure of structural recovery.

3.6.1. Moment Capacity Comparison Ratio

To compare the moment capacity of the repaired specimen with that of the original specimen, the moment capacity comparison ratio η_M is defined as:

$$\eta_M = \frac{M_{u,R1}}{M_{u,T2}} \times 100\% \quad (1)$$

where $M_{u,R1}$ is the peak moment of the repaired specimen R1, and $M_{u,T2}$ is the peak moment of the original specimen T2.

Based on the experimental results, the moment capacity comparison ratio of specimen R1 is 115.9%, indicating that the repaired welded end-plate connection achieved a peak moment approximately 15.9% higher than that of the original T-stub joint. This increase is mainly attributed to the modification of the connection configuration. In specimen T2, the blind-bolted T-stub connection exhibits interface slip and local deformation of the T-stub connector during cyclic loading, which reduce the efficiency of force transfer. After repair, the connection is reconstructed using a welded end-plate bolted hybrid system, providing a stiffer load-transfer path and reducing the influence of interface slip. Consequently, a higher peak moment capacity is achieved.

3.6.2. Stiffness Comparison Ratio

To compare the rotational stiffness of the repaired specimen with that of the original specimen, the stiffness comparison ratio η_K is defined as:

$$\eta_K = \frac{K_{R1}}{K_{T2}} \times 100\% \quad (2)$$

where K_{R1} is the secant stiffness of the repaired specimen R1; and K_{T2} is the secant stiffness of the original specimen T2 at the same loading stage.

Based on the experimental results, the initial secant stiffness of specimen R1 was 3891.11 kN·m·rad^{-1}, which exceeded that of specimen T2 (3172.98 kN·m·rad^{-1}), corresponding to a stiffness comparison ratio of 122.6%. At the later loading stage, the secant stiffness values of R1 and T2 were 1773.39 kN·m·rad^{-1} and 1451.62 kN·m·rad^{-1} respectively, resulting in a stiffness comparison ratio of 122.2%. The results indicate that the repaired joint maintained consistently higher stiffness throughout the loading process, with the stiffness comparison ratio remaining above 120%. This improvement is primarily attributed to the replacement of the original blind-bolted T-stub connection with a welded end-plate bolted hybrid connection. The modified connection configuration reduced interface slip and enhanced rotational restraint, thereby increasing both the initial stiffness and the overall stiffness of the joint during cyclic loading.

3.6.3. Energy Dissipation Comparison Ratio

To compare the energy dissipation capacity of the repaired specimen with that of the original specimen, the cumulative energy dissipation at the same loading stage was evaluated using the energy dissipation comparison ratio η_E, defined as:

$$\eta_E = \frac{W_{R1}}{W_{T2}} \times 100\% \quad (3)$$

where W_{R1} is the cumulative energy dissipation of the repaired specimen R1, and W_{T2} is the cumulative energy dissipation of the original specimen T2 at the same loading stage.

The comparison results indicate that the cumulative energy dissipation of specimen R1 increased continuously throughout the loading process and exceeded that of the original specimen T2 at large deformation levels. At the final loading stage, the cumulative energy dissipation values of R1 and T2 reached 12.856 kJ and 8.69 kJ, respectively, corresponding to an energy dissipation comparison ratio of 147.9%. The enhanced energy dissipation performance of the repaired joint can be attributed to the change in connection configuration. After repair, the load transfer mechanism shifted from a blind-bolted T-stub connection to a welded end-plate connection. During cyclic loading, plastic deformation developed primarily in the end-plate and weld regions. Although interface slip caused more pronounced pinching, specimen R1 maintained higher resisting forces and relatively stable equivalent viscous damping ratios at large deformation levels. These characteristics resulted in greater cumulative energy dissipation over the complete loading history.

It should be noted that the comparison ratios of moment capacity, stiffness, and energy dissipation exceeded 100% because specimens T2 and R1 employed different connection configurations. Therefore, values greater than 100% indicate that the repaired welded end-plate connection exhibited higher corresponding performance than the original blind-bolted T-stub connection. These ratios are intended only for performance comparison between the two connection types and should not be interpreted as indicators of the restoration of the original blind-bolted T-stub joint.

Although the repaired specimen R1 exhibited superior mechanical performance, this does not mean that the welded end-plate configuration should directly replace the original T-stub joint design. The primary objective of the blind-bolted T-stub connection is to provide a prefabricated and replaceable connection solution for steel MCTBs, where seismic damage can be concentrated in replaceable components while protecting the primary beam and column members. During the repair process, direct replacement of the damaged T-stub and blind bolts was initially considered. However, the internal leveling plates inside the closed-section transition column could not be accurately repositioned after cyclic loading, making the reuse of the original blind-bolted connection impractical. Therefore, the welded end-plate connection was adopted as an alternative repair strategy. Nevertheless, the repaired joint maintained stable hysteretic behavior and satisfactory deformation capacity, demonstrating that the proposed repair strategy provides an effective alternative for post-earthquake rehabilitation of damaged blind-bolted T-stub joints. These results confirm the feasibility of using welded end-plate connections for the post-earthquake rehabilitation of prefabricated blind-bolted T-stub joints.

4. Numerical Analysis

4.1. Finite Element Modeling

4.1.1. Modeling and Meshing

To further investigate the mechanical behavior and energy dissipation mechanism of the prefabricated single beam–column joints in steel MCTBs, a finite element (FE) model was developed in ABAQUS 2016 and validated against the experimental results. The geometrical configurations of the original specimen T2 and repaired specimen R1 were reproduced according to the experimental dimensions, as shown in Figure 14. All steel components were modeled using eight-node linear brick elements with reduced integration (C3D8R). The adopted FE modeling strategy was established based on both previous studies on steel traditional-style building structures and representative international studies on

beam–column connections. Previous studies have successfully employed refined ABAQUS models with C3D8R solid elements to simulate steel traditional-style building joints and steel frames [2–8]. The modeling approaches for blind-bolted T-stub connections, end-plate connections, and blind-bolt assemblies have also been verified in previous experimental and numerical studies [20–22]. In addition, the applicability of C3D8R solid elements has also been demonstrated in nonlinear ABAQUS analyses of reinforced concrete beam–column joints subjected to reversed cyclic loading [42]. Therefore, the present FE model was established based on these validated modeling strategies while considering the specific characteristics of the blind-bolted T-stub and repaired end-plate connections.

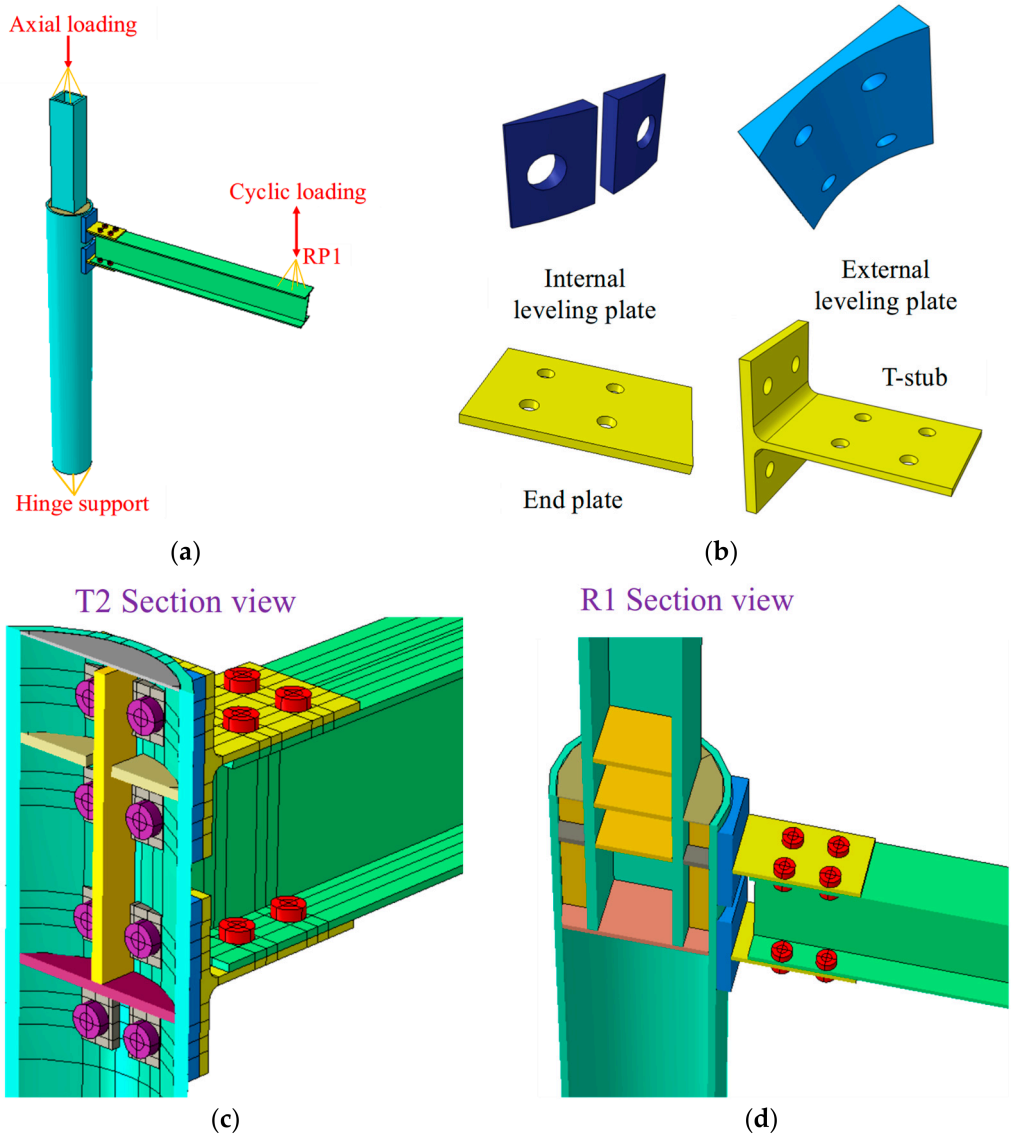


Figure 14. Finite element model. (**a**) Assembly view; (**b**) Component view; (**c**) T2 section view; (**d**) R1 section view.

Considering the complex stress distribution and plastic deformation in the joint region, mesh refinement was applied to the T-stub connectors, blind bolt holes, and beam–column connection zone. The mesh size in these critical regions was controlled within 5 mm, whereas a relatively coarse mesh of 10–15 mm was adopted for the remaining regions to improve computational efficiency. The mesh configuration of the FE models is shown in Figure 15.

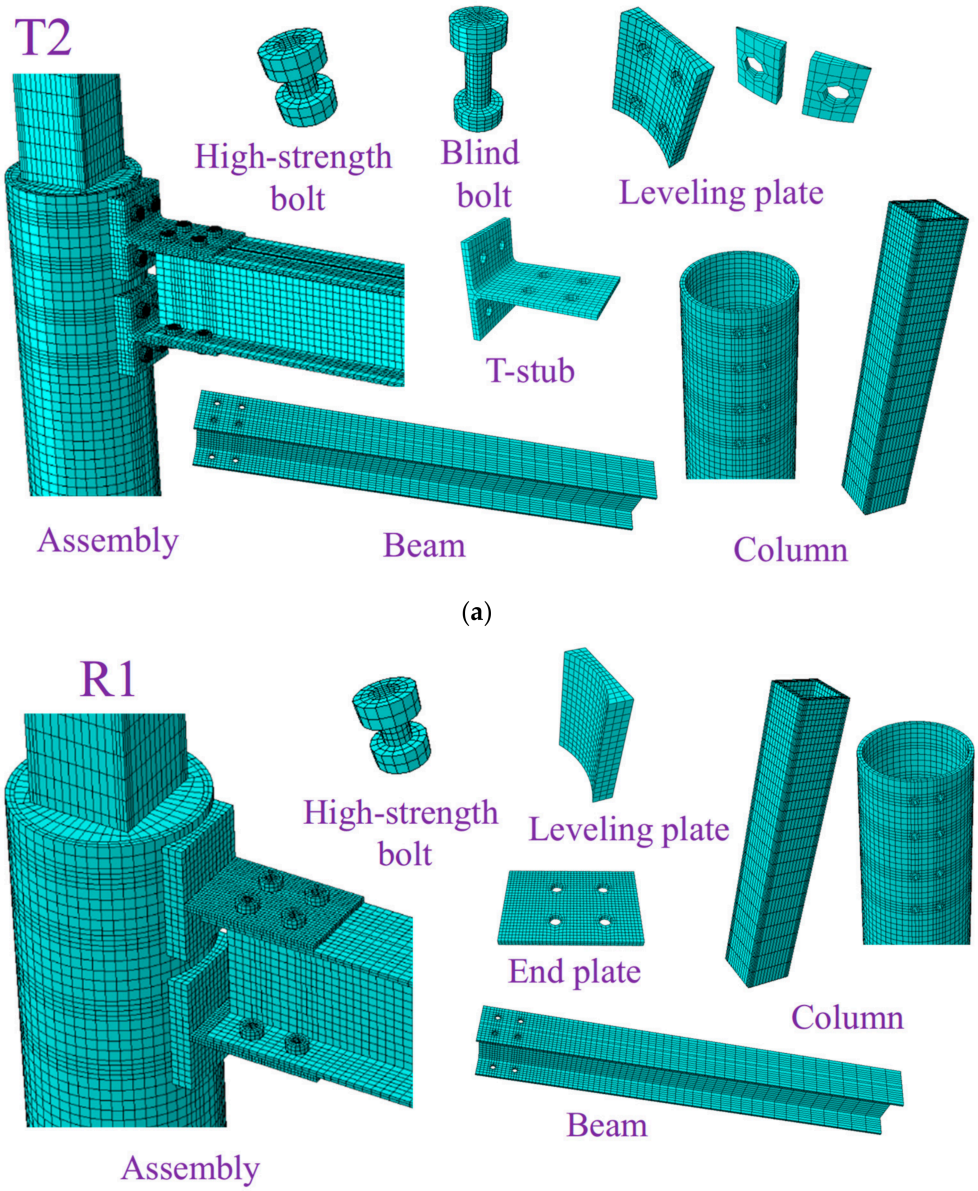


Figure 15. Mesh diagram. (**a**) T2; (**b**) R1.

4.1.2. Constitutive Relationship

The steel material properties used in the FE model were determined based on the coupon test results presented in Section 2.3. Considering that the plastic deformation observed in the experiments was mainly concentrated in the T-stub connectors and end-plate regions, while the CHS column and H-shaped beams remained almost elastic, two different constitutive models were adopted to balance computational efficiency and accuracy.

For the T-stub connectors and welded end-plate components, a simplified three-line constitutive model proposed in previous studies [3–7] was adopted to simulate the cyclic elastic–plastic behavior, as shown in Figure 16a. The yield stress, ultimate tensile stress, and corresponding strain values were determined according to the measured material properties from coupon tests. For the CHS columns and H-shaped beams, which experienced negligible plastic deformation during the tests, an ideal elastic–plastic constitutive model was adopted, as shown in Figure 16b.

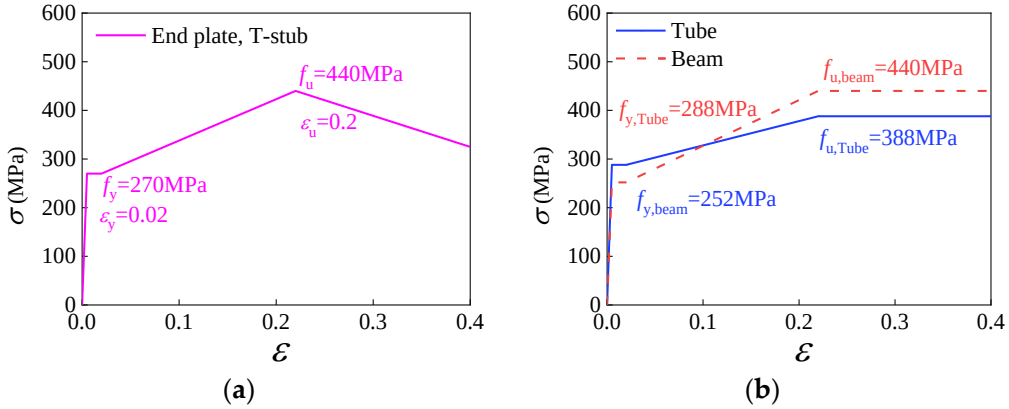


Figure 16. Constitutive models of steel. (**a**) End plate and T-stub; (**b**) Tube and Beam.

In both constitutive models, the elastic modulus and Poisson's ratio were taken as 2.07×10^5 MPa and 0.3, respectively. The steel yielding behavior was described using the von Mises yield criterion combined with the combined isotropic–kinematic hardening model and associated flow rule. The von Mises yield function is expressed as Equation (4), where σ_1, σ_2, and σ_3 represent the first, second, and third principal stresses, respectively.

$$\sigma_e = \sqrt{\frac{1}{2}\left[(\sigma_1 - \sigma_2)^2 + (\sigma_2 - \sigma_3)^2 + (\sigma_3 - \sigma_1)^2\right]} \quad (4)$$

4.1.3. Boundary Conditions and Loading Procedure

Surface-to-surface contact interactions were defined between all contacting components. The welded regions between the connected steel components were simulated using the Tie constraint to represent the welded connection behavior. To reproduce the experimental support condition, a reference point was established 200 mm below the column base, corresponding to the center position of the hinged support in the test setup. The reference point was coupled with the column base using a distributing coupling constraint and was defined as a hinge support. The translational degrees of freedom U1, U2, and U3 and rotational degrees of freedom UR2 and UR3 were restrained. Hard contact was adopted in the normal direction, while the tangential behavior was modeled using the Coulomb friction law with a friction coefficient of 0.30. Hard contact was also assigned between the bolt shank and the hole surface to simulate force transfer through bearing action. The pretension force in the high-strength bolts was simulated using the Pretension Section technique. To ensure numerical stability and convergence, the bolt pretension was applied in two stages. An initial pretension force of 50 kN was first introduced, followed by the design pretension force of 190 kN. Subsequently, the bolt length was fixed using the Fix at Current Length option to maintain the pretension force during the cyclic loading analysis.

The loading procedure was divided into four analysis steps. In the first step, boundary conditions were established and bolt pretension forces were applied to simulate the initial assembly state. In the second step, the "Fix at Current Length" option was adopted to maintain the bolt pretension force during cyclic loading. In the third step, the constant axial load of 275 kN was applied through the reference point at the column top. Finally, the cyclic displacement loading protocol was imposed at the beam-end reference point according to the experimental loading history.

4.2. Stress Distribution Comparison

The von Mises stress contours of specimens T2 and R1 at the yielding and peak-load states are shown in Figure 17a–d. As shown in Figure 17a,b, the high-stress regions of specimen T2 were mainly concentrated in the T-stub connector. The maximum stress

occurred at the flange–web junction of the T-stub. As the loading level increased from the yielding state to the peak-load state, the stress concentration region gradually expanded and developed into a pronounced plastic zone. The locations of stress concentration predicted by the finite element model agreed well with the crack initiation and final fracture locations observed in the experiment, indicating that the flange–web junction of the T-stub served as the primary energy-dissipation and damage zone of the joint.

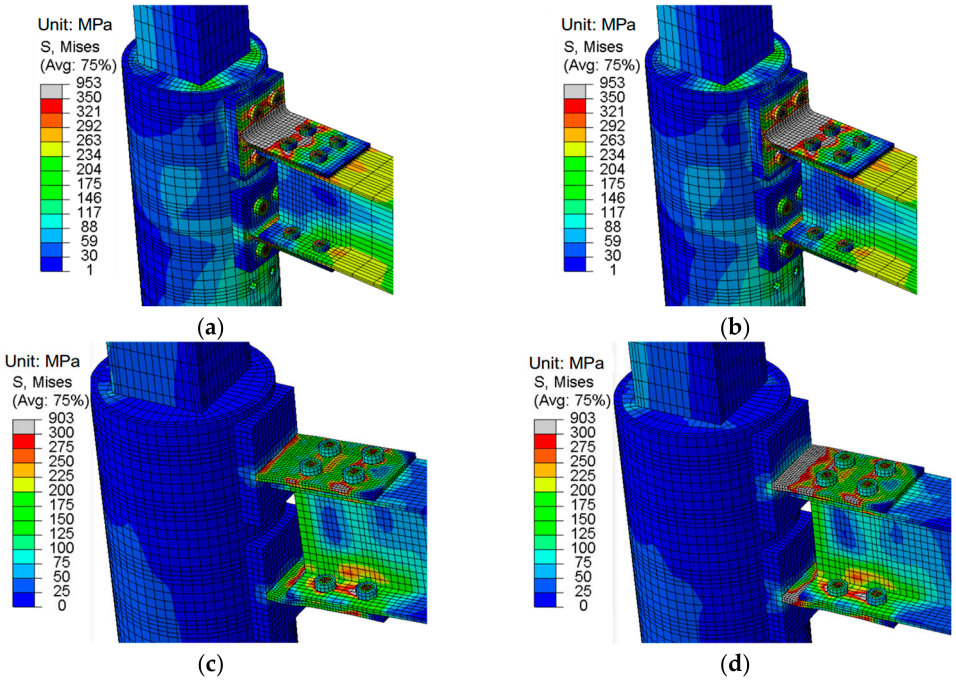


Figure 17. Von Mises stress distribution of specimens T2 and R1. (**a**) T2 at yield state; (**b**) T2 at peak load; (**c**) R1 at yield state; (**d**) R1 at peak load.

For the repaired specimen R1, the stress distribution is shown in Figure 17c,d. The high-stress regions were mainly distributed in the end-plate connection region and the adjacent welds. Compared with specimen T2, the load transfer path changed after repair, resulting in a shift of stress concentration from the T-stub connector to the end-plate connection region. As the loading level increased, the stress concentration in the end-plate and weld regions became more pronounced, whereas the beam and column members remained at relatively low stress levels throughout the loading process. This result indicates that damage was still effectively concentrated within the connection region after repair.

Figure 18a compares the deformation pattern of the T-stub connector obtained from the finite element analysis with that observed in the experiment. Under beam-end bending action, significant deformation developed in the T-stub flange, particularly near the flange–web junction. The deformation pattern predicted by the finite element model was consistent with the experimental observations, demonstrating that the proposed model was capable of accurately reproducing the deformation characteristics of the connection. Figure 18b shows the relative slip deformation around the blind-bolt hole region. As the loading level increased, noticeable relative displacement developed between the blind bolt and the surrounding hole surface, accompanied by local bearing deformation around the bolt hole. This phenomenon indicates that cumulative slip and local deformation occurred in the connection region under cyclic loading, which agrees well with the experimental observations. Overall, the finite element model successfully reproduced the stress distribution, deformation characteristics, and local slip behavior observed in the

experiments, demonstrating its reliability for subsequent analysis of the seismic behavior and post-earthquake repair performance of the proposed joints.

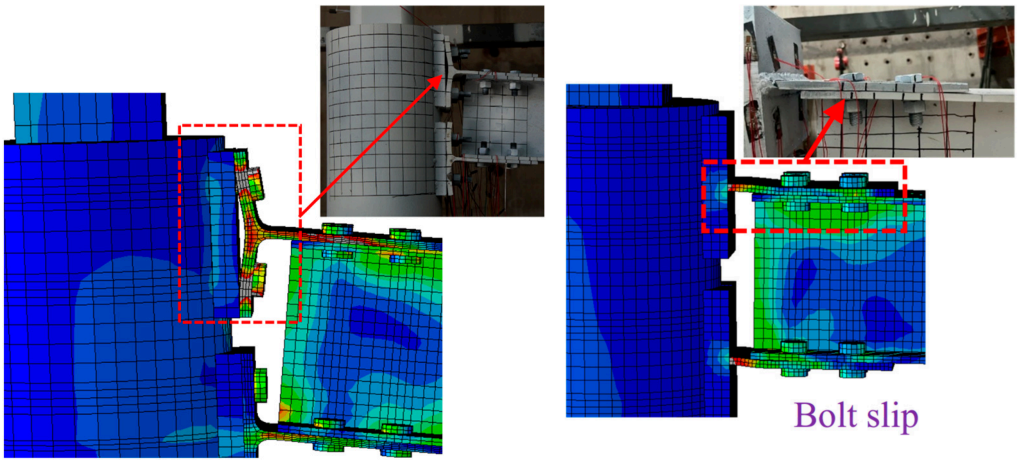


Figure 18. Comparison between experimental and FE results. (**a**) T-stub deformation; (**b**) End-plate deformation and bolt slip.

4.3. Comparison of Hysteretic and Skeleton Curves

To validate the reliability of the finite element model, the experimental and numerical results of the original specimen T2 and the repaired specimen R1 were compared, as shown in Figure 19. For specimen T2, the numerical hysteretic curves agreed well with the experimental results. Both sets of curves exhibited typical bow-shaped hysteretic behavior accompanied by moderate pinching effects. As the rotation amplitude increased, the experimental and numerical results showed similar stiffness degradation characteristics and strength evolution trends. The peak moment predicted by the finite element model was close to the experimental value, indicating that the model accurately captured the cyclic response and energy dissipation behavior of the blind-bolted T-stub joint. For the repaired specimen R1, the finite element results also reproduced the main features of the experimental hysteretic response. The pinching behavior observed in the tests, which was associated with plastic deformation in the end-plate connection region and slip at the bolted interfaces, was reasonably reflected in the numerical results. With increasing displacement amplitude, both the experimental and numerical curves exhibited similar stiffness degradation patterns and strength development trends, demonstrating that the proposed model was capable of simulating the cyclic behavior of the repaired joint.

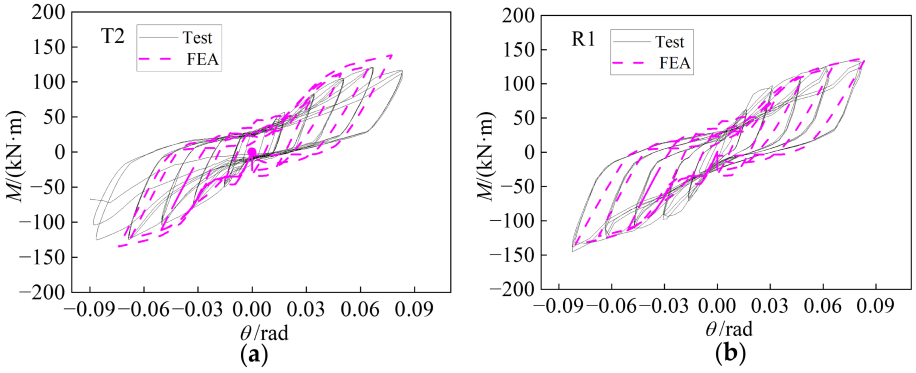


Figure 19. Comparison of hysteresis curves. (**a**) T2; (**b**) R1.

The comparison of the skeleton curves further confirmed the accuracy of the finite element model. For both T2 and R1, the numerical predictions showed good agreement

with the experimental results in terms of initial stiffness, peak moment capacity, and post-peak degradation behavior. The overall evolution trends of the skeleton curves were reproduced satisfactorily throughout the loading process. Overall, good agreement was achieved between the experimental and numerical results with respect to hysteretic response, skeleton curve characteristics, peak strength, stiffness degradation, and energy dissipation behavior. The minor discrepancies observed between the two sets of results may be attributed to factors such as material imperfections, fabrication tolerances, installation errors, and welding residual stresses that were not fully considered in the numerical model. These results demonstrate that the proposed finite element model can accurately represent the seismic behavior of both the original and repaired joints and can therefore be used for subsequent parametric studies and mechanism analysis.

5. Conclusions

This study investigated the seismic behavior of blind-bolted T-stub beam–column joints in steel MCTBs and compared the seismic performance of the original and repaired joints. Two original specimens and one repaired specimen were tested under low-cycle reversed loading, and validated finite element models were developed for further analysis. The main conclusions are summarized as follows:

(1) The blind-bolted T-stub joint exhibited a desirable damage-control mechanism. Under cyclic loading, plastic deformation and damage were primarily concentrated in the T-stub connector, while the beam, column, and leveling plates remained essentially intact. Failure occurred mainly at the flange–web junction of the T-stub, demonstrating that the connection acted as the designated energy-dissipating component and providing favorable conditions for post-earthquake repair.

(2) The original joints exhibited stable hysteretic behavior, satisfactory ductility, and good energy dissipation capacity. Increasing the T-stub web thickness from 8 mm to 9 mm improved both the moment capacity and ductility of the joint, indicating that an appropriate increase in T-stub stiffness can enhance seismic performance.

(3) The FE model reasonably reproduced the hysteretic response, stiffness degradation, deformation characteristics, and local slip behavior observed in the experiments. The predicted stress concentration regions were consistent with the experimentally observed damage locations, demonstrating the capability of the proposed numerical model to capture the main mechanical behavior of the investigated joints.

(4) The proposed repair strategy demonstrated the feasibility of rehabilitating damaged blind-bolted T-stub joints by replacing the damaged connection with a welded end-plate connection. The repaired specimen exhibited stable hysteretic behavior and maintained a ductility coefficient of 2.61, although the failure mode changed from T-stub fracture to weld fracture after repair.

(5) For the repaired specimen R1, the end-plate replacement connection exhibited higher moment capacity, stiffness, and cumulative energy dissipation than the original T-stub joint. The corresponding moment capacity ratio, stiffness ratio, and energy dissipation ratio reached 115.9%, more than 120%, and 147.9%, respectively. The primary beam and column members remained essentially undamaged, demonstrating the feasibility of the proposed repair strategy for the investigated repair configuration.

This study made a preliminary attempt to investigate the post-earthquake repair performance of prefabricated blind-bolted T-stub joints in steel MCTBs. Although the proposed welded end-plate connection provided an effective repair solution, more efficient bolt-based replaceable repair configurations remain to be developed in future work. Improving the connection reliability of the internal leveling plate may enable direct replacement of damaged T-stub connectors without additional welding work. Future work will

also investigate the influence of different axial load ratios on the seismic performance and repair behavior of the proposed joints.

Author Contributions: Conceptualization, Z.W.; methodology, X.W.; writing—original draft preparation, Z.W.; writing—review and editing, F.L. and X.Z.; software, J.D.; supervision, H.S. and F.L.; project administration, X.W.; funding acquisition, X.W. All authors have read and agreed to the published version of the manuscript.

Funding: This work was supported by the National Natural Science Foundation of China (Grant No. 52008330), the Natural Science Foundation of Henan Province (Grant No. 252300421260), and the Joint Fund for Science and Technology Research Projects of Henan Province (Grant No. 252103810049). This work was also supported by the Major Science and Technology Program of Hainan Province (Grant No. ZDKJ201803).

Data Availability Statement: The original contributions presented in this study are included in the article. Further inquiries can be directed to the corresponding author.

Conflicts of Interest: The authors declare that they have no conflicts of interest.

References

1. Qi, L.; Cao, Y.; Xue, J.; Yuan, Z.; Ling, H.; Meng, R. Seismic performance evaluation and engineering application of modern Chinese traditional-style buildings: State-of-the-art review. *Structures* **2023**, *56*, 105022. [CrossRef]
2. Qi, L.; Xue, J.; Qi, L.; Leon, R.T. Experimental and analytical investigation of transition steel connections in traditional-style buildings. *Eng. Struct.* **2017**, *150*, 438–450. [CrossRef]
3. Wu, Z.; Wang, X.; Bu, X.; Dong, J. Design and Shear Bearing Capacity Calculation of All-Welded Irregular Joints in Steel Traditional Chinese Buildings. *Buildings* **2025**, *15*, 184. [CrossRef]
4. Qi, L.; Xue, J. Pseudo-dynamic test and time-history analyses of traditional-style steel frame structures. *Int. J. Steel Struct.* **2018**, *18*, 402–416. [CrossRef]
5. Qi, L.; Xue, J.; Sui, Y.; Wu, Z. Smart retrofitting of irregular steel joints in traditional Chinese buildings by viscous dampers. *Eng. Struct.* **2021**, *228*, 111526. [CrossRef]
6. Yuan, Z.; Qi, L.; Xue, J. Seismic performance of steel semi-rigid friction-damped joints with replaceable angles in modern Chinese traditional-style buildings. *J. Constr. Steel Res.* **2023**, *207*, 107948. [CrossRef]
7. Yuan, Z.; Qi, L.; Xue, G.; Xue, J. Resilient joints with SMA bar-shear friction damper (SSFD) device in steel modern Chinese traditional-style buildings: Seismic performance evaluation and optimized design. *J. Build. Eng.* **2024**, *82*, 108300. [CrossRef]
8. Qi, L.; Yuan, Z.; Xue, J. Experimental and numerical study on seismic performance of steel semi-rigid joints equipped with SMA bars and friction dampers. *Eng. Struct.* **2024**, *301*, 117320. [CrossRef]
9. Menge, B.Y.; Aure, T.W. Seismic Performance Evaluation of Steel Beam-to-Concrete Confined with FRP Tube Column Connections. *Asian J. Civ. Eng.* **2022**, *23*, 665–693. [CrossRef]
10. Tizani, W.; Mahmood, M.; Dionysios, B. Effect of concrete infill and slenderness on column-face component in anchored blind-bolt connections. *J. Struct. Eng.* **2020**, *146*, 04020039. [CrossRef]
11. Cabrera, M.; Tizani, W.; Mahmood, M.; Shamsudin, M.F. Analysis of extended Hollo-Bolt connections: Combined failure in tension. *J. Constr. Steel Res.* **2020**, *165*, 105776. [CrossRef]
12. Cabrera, M.; Tizani, W.; Ninic, J.; Wang, F. Experimental and numerical analysis of preload in extended Hollo-Bolt blind bolts. *J. Constr. Steel Res.* **2021**, *186*, 106885. [CrossRef]
13. Ali, A.M.; Masmoudi, R. Experimental and Analytical Investigation of New Concrete-Filled FRP Tube Beam–Column Connections. *Eng. Struct.* **2019**, *191*, 311–322. [CrossRef]
14. Cabrera, M.; Tizani, W.; Ninic, J. A Review and Analysis of Testing and Modeling Practice of Extended Hollo-Bolt Blind Bolt Connections. *J. Constr. Steel Res.* **2021**, *183*, 106763. [CrossRef]
15. Dhanapal, J.; Das, S.; Ghaednia, H.; Bell, M. Experimental study on structural performance of flow drilled connections in HSS members. *J. Constr. Steel Res.* **2020**, *164*, 105786. [CrossRef]
16. Lee, J.; Goldsworthy, H.; Gad, E. Blind bolted T-stub connections to unfilled hollow section columns in low-rise structures. *J. Constr. Steel Res.* **2010**, *66*, 981–992. [CrossRef]
17. Lee, J.; Goldsworthy, H.; Gad, E. Blind bolted moment connection to unfilled hollow section columns using extended T-stub with back-face support. *Eng. Struct.* **2011**, *33*, 1710–1722. [CrossRef]
18. Wang, W.; Li, M.; Chen, Y.; Jian, X. Cyclic behavior of endplate connections to tubular columns with novel slip-critical blind bolts. *Eng. Struct.* **2017**, *148*, 949–962. [CrossRef]

19. Tizani, W.; Rahman, N.A.; Pitrakkos, T. Fatigue Life of an Anchored Blind-Bolt Loaded in Tension. *J. Constr. Steel Res.* **2014**, *93*, 1–8. [CrossRef]
20. Prinz, G.S.; Nussbaumer, A.; Borges, L.; Khadka, S. Experimental Testing and Simulation of Bolted Beam–Column Connections Having Thick Extended Endplates and Multiple Bolts per Row. *Eng. Struct.* **2014**, *59*, 434–447. [CrossRef]
21. Cho, B.H.; Lee, J.S.; Kim, H.; Lee, J.H.; Kim, D.K. Structural Performance of a New Blind-Bolted Frame Modular Beam–Column Connection under Lateral Loading. *Appl. Sci.* **2019**, *9*, 1929. [CrossRef]
22. Fan, J.; Zhao, J. Moment-rotation model of composite connection with curved endplate and blind bolts. *J. Constr. Steel Res.* **2021**, *185*, 106840. [CrossRef]
23. Liu, H.; Yan, S.; Wang, X.; Zhang, J.; Lin, Y. Experimental study on the seismic damage behavior of composite joints of concrete-filled steel tube column with blind bolts. *Structures* **2024**, *70*, 107767. [CrossRef]
24. Xiao, S.; Bu, X.; Chen, Y.; Wang, X. Investigating the damage-based seismic performance of the blind bolt-connected steel framework. *Structures* **2024**, *69*, 107388. [CrossRef]
25. Abidelah, A.; Bouchaïr, A.; Kerdal, D.E. Experimental and Analytical Behavior of Bolted End-Plate Connections with or without Stiffeners. *J. Constr. Steel Res.* **2012**, *76*, 13–27. [CrossRef]
26. Men, J.; Li, T.; Zhou, Q.; Zhang, H.; Huang, C. Structural fuse performance and earthquake-resilient performance of beam-column joints with replaceable T-stub. *J. Constr. Steel Res.* **2023**, *206*, 107943. [CrossRef]
27. Li, T.; Men, J.; Zhang, Q.; Li, J.; Huang, C. Seismic fragility and resilience assessment of steel frame with replaceable T-stub connection components. *Eng. Struct.* **2024**, *314*, 118396. [CrossRef]
28. Chen, P.; Pan, J.; Hu, F.; Wang, Z. Experimental investigation on earthquake-resilient steel beam-to-column joints with replaceable buckling-restrained fuses. *J. Constr. Steel Res.* **2022**, *196*, 107413. [CrossRef]
29. Yan, T.; Chung, Y.; Jin, J.; Lin, K.; Komatsu, Y.; Nagae, T. Full-scale tests on resilient post-earthquake repair of steel beam-to-column connections. *J. Build. Eng.* **2025**, *108*, 112845. [CrossRef]
30. Chen, Y.; Lu, Y.; Liu, T. Seismic performance of precast steel beam-column joint with bolted connection. *Buildings* **2024**, *14*, 2588. [CrossRef]
31. Meng, B.; You, K.; Yang, B.; Kong, D.; Wen, J. Anti-Progressive Collapse Performance and Design Method of Novel T-Stub Connections. *Eng. Struct.* **2024**, *319*, 118880. [CrossRef]
32. Jeddi, M.Z.; Sulong, N.H.R.; Ghanbari-Ghazijahani, T. Behaviour of Double-Sleeve TubeBolt Moment Connections in CFT Columns under Cyclic Loading. *J. Constr. Steel Res.* **2022**, *194*, 107302. [CrossRef]
33. Tizani, W.; Wang, Z.Y.; Hajirasouliha, I. Hysteretic Performance of a New Blind-Bolted Connection to Concrete-Filled Columns under Cyclic Loading: An Experimental Investigation. *Eng. Struct.* **2013**, *46*, 535–546. [CrossRef]
34. Park, K.S.; Moon, J.; Lee, S.S.; Kim, D.K.; Kim, H.S. Embedded Steel Column-to-Foundation Connection for a Modular Structural System. *Eng. Struct.* **2016**, *110*, 244–257. [CrossRef]
35. Fan, L.; Guo, Z.; Wang, X.; Yu, Y.; Wu, Z.; Sun, H.; Zhang, D.; Jia, X. Seismic performance of steel side joints of T-stub connectors in antique buildings. *J. Henan Univ. Sci. Technol. (Nat. Sci.)* **2025**, *46*, 69–78, 121–122.
36. Li, J. *The Construction Method*; Commercial Press: Shanghai, China, 1932.
37. *GB 50017-2017*; Standard for Design of Steel Structures. China Architecture & Building Press: Beijing, China, 2017.
38. *GB 50011-2010*; Code for Seismic Design of Buildings. China Architecture & Building Press: Beijing, China, 2010.
39. *GB 50205-2020*; Standard for Acceptance of Construction Quality of Steel Structures. China Architecture & Building Press: Beijing, China, 2020.
40. *GB/T 228.1-2010*; Metallic Materials—Tensile Testing—Part 1: Method of Test at Room Temperature. Chinese Standard Press: Beijing, China, 2010.
41. *EN 1993-1-8*; Eurocode 3: Design of Steel Structures-Part 1-8: Design of Joints. European Committee for Standardization (CEN): Brussels, Belgium, 2005.
42. Pekgökgöz, R.K.; Avcil, F. Effect of Steel Fibres on Reinforced Concrete Beam-Column Joints under Reversed Cyclic Loading. *Građevinar* **2021**, *73*, 1185–1194.

Disclaimer/Publisher's Note: The statements, opinions and data contained in all publications are solely those of the individual author(s) and contributor(s) and not of MDPI and/or the editor(s). MDPI and/or the editor(s) disclaim responsibility for any injury to people or property resulting from any ideas, methods, instructions or products referred to in the content.